



A nose-to-brain axis for spoiled food odor-triggered defensive responses in male mice

Received: 17 April 2025

Accepted: 16 December 2025

Published online: 03 January 2026

 Check for updates

Wan-Ying Dong^{1,2,10}, Ping-Kai Cheng^{2,10}, Jun-Hao Miao^{2,10}, Pei Shi^{2,3,10}, Ji-Ye Huang², Yu-Xin Jin², Qian-Qian Lou², Haitao Wang⁴, Zerui Wang⁵, Wan Zhao⁶, Zhi Zhang^{2,7,8}  , Wei Wang^{1,2}  , Qi-Xin Zhou⁹   & Xia Zhu^{2,7}  

Rancid odors can trigger retching and aversion in humans that prevent consumption of spoiled food, and consequently metabolic dysregulation, but the underlying neural mechanisms remain unclear. Here, we show that exposure to 2-methylbutyric acid (2MBA) odor triggers such defensive responses in male mice, mediated by a nose-to-brain axis. 2MBA perception in olfactory epithelium activates neurons in olfactory bulb (OB) projecting to glutamatergic neurons in anterior piriform cortex (aPir^{Glu}), which in turn project to either the mediodorsal thalamic nucleus (MD), which innervates respiratory muscles to drive retching-like behaviors, or project to the nucleus accumbens (NAC) to drive aversion. Artificial inhibition of the nose→OB→aPir→MD^{Glu}→respiratory muscles circuit diminishes retching-like behaviors, but not aversion, while inhibiting the nose→OB→aPir→NAC circuit diminishes aversion, but not retching-like behaviors. These findings thus establish a nose-to-brain axis for rancid odor-triggered retching and aversion in male mice, advancing our understanding of sensory-motor integration and whole-body neural bases of defensive responses to odor.

Olfactory perception is required for maintaining metabolic homeostasis, and has been proposed as a potential dietary intervention for treating metabolic disorders based on evidence that normal food odors could regulate lipid mobilization and insulin resistance^{1–3}. In humans, spoiled food odors can signal warnings of health risks and trigger defensive response behaviors, such as vomiting, retching, or diarrhea to empty noxious chemicals from the gastrointestinal tract, or aversion that prevents ingestion of noxious substances^{4,5}. Based on their effects in reducing or avoiding infection and poisoning, these

odor-inducible behaviors can effectively mitigate metabolic burden on hepatic detoxification pathways and preserve renal clearance capacity^{6–8}.

Olfactory perception begins with scent molecules binding to receptors on olfactory sensory neurons in specialized tissue of the nasal cavity known as the olfactory epithelium; the axons of these neurons converge in small spherical structures known as glomeruli in the olfactory bulb (OB)^{9,10}. Although a topological pattern of activated glomeruli has been identified as a basis for distinguishing different

¹Department of Endocrinology and Metabolism, The First Affiliated Hospital of USTC, Division of Life Sciences and Medicine, University of Science and Technology of China, Hefei, China. ²Department of Biophysics and Neurobiology, Division of Life Sciences and Medicine, University of Science and Technology of China, Hefei, China. ³Department of Anesthesiology, Linyi People's Hospital, Linyi, China. ⁴College & Hospital of Stomatology, Anhui Medical University, Key Laboratory of Oral Diseases Research of Anhui Province, Hefei, China. ⁵Hefei No.1 High School, Hefei, China. ⁶Department of Otolaryngology-Head and Neck Surgery, The First Affiliated Hospital of USTC, Division of Life Sciences and Medicine, University of Science and Technology of China, Hefei, China. ⁷Department of Pain Medicine, The First Affiliated Hospital of Anhui Medical University, Hefei, China. ⁸Department of Anatomy, Anhui Provincial Key Laboratory for Brain Bank Construction and Resource Utilization, School of Basic Medical Sciences, Anhui Medical University, Hefei, China. ⁹Key Laboratory of Animal Models and Human Disease Mechanisms, and Laboratory of Learning and Memory, Kunming Institute of Zoology, The Chinese Academy of Sciences, Kunming, China. ¹⁰These authors contributed equally: Wan-Ying Dong, Ping-Kai Cheng, Jun-Hao Miao, Pei Shi. ✉ e-mail: zhizhang@ustc.edu.cn; hfw2001@ustc.edu.cn; qixin_zhou@vip.126.com; xiaozhu@ustc.edu.cn

smells^{9,10}, little is known about how such topographical information from the OB is transmitted and subsequently interpreted in the brain to spoiled food odors.

Output cells of the OB relay information from individual glomeruli to olfactory cortical areas, the largest of which is the piriform cortex (Pir), via diffuse and overlapping projections, thus allowing individual Pir neurons to incorporate inputs from different combinations of glomeruli^{11,12}. The anterior and posterior Pir (aPir and pPir) exhibit neuroanatomical differences, with the aPir receiving more extensive inputs from OB than pPir¹³. The aPir in turn sends projections to numerous brain regions associated with defensive responses, including the prefrontal cortex^{14,15}. However, it remains unclear whether and how the OB-aPir pathway participates in defensive responses to spoiled food odors.

The neural mechanism underlying vomiting triggered by spoiled food odors has been difficult to resolve, as the emetic species (e.g., cat, dog, ferret) used in traditional paradigms for this research have relatively fewer experimental resources for detailed molecular and cellular investigations compared to mice^{16–18}, such as the capacity for straightforward genetic manipulation and the broad availability of transgenic strains¹⁹. Although laboratory mice lack vomiting behavior because the smooth muscle of the esophagus is not strong enough to expel food from the gastrointestinal tract, they do exhibit retching-like behavior, which has been used in recent studies to investigate vomiting-related responses^{6,19}.

In the present study, we found that exposure to 2-methylbutyric acid (2MBA), a rancid odor associated with spoiled food²⁰, triggers a retching-like behavior in male mice, which could promote emptying noxious chemicals, as well as aversion behaviors that could prevent consumption of potentially harmful substances. Through a combination of viral tracing, in vivo multi-tetrode electrophysiological recordings, and microendoscopic calcium imaging, we subsequently characterized the organization of a nose→OB→anterior piriform cortex (aPir)→mediodorsal thalamic nucleus→respiratory muscles circuit that is activated by exposure to 2MBA odor and triggers retching-like behavior in mice. We also uncovered a nose→OB→aPir→accumbens nucleus circuit that is activated in parallel and mediates a conditioned aversion to 2MBA odor in mice. Beyond defining the afferent to efferent pathway of a circuit mechanism for sensory-motor integration and periphery-brain communication, the present study provides a conceptual basis for developing odor-based therapies and intranasal neuromodulation strategies aimed at maintaining metabolic homeostasis or treating metabolic disorders.

Results

2-methylbutyric acid (2MBA)-triggered retching-like behavior and aversion in male mice

Inspired by human defensive response to unpleasant odors, we established a male mouse paradigm for odor-triggered retching-like behavior. Specifically, filter papers were individually placed in the center of a box. Several unpleasant odorants, including 2-methylbutyric acid (2MBA), (+)-fenchone (FEN), hexanol (HEX), limonene (LIM)²¹, predator-associated odor (trimethylthiazoline, TMT)²², bacterial metabolite odor (hydrogen sulfide, H₂S)²³, and bacterial virulence- and antibiotic resistance-associated odor (MgrB)²⁴ at different concentrations (diluted with ddH₂O), were each pipetted onto a filter paper and left to evaporate in respective boxes. Mice were placed within the box and permitted to move freely during a 20 min odor inhalation phase, while a camera was positioned horizontally outside the box to record their behaviors (Fig. 1a). Among these treatments, only exposure to 2MBA, a rancid odor associated with spoiled food, triggered significant mouth-opening actions analogous to retching behavior in humans, while none of the other unpleasant odorants, nor the ddH₂O control, triggered such behavior (Fig. 1b–d, Supplementary Figs. 1 and 2, and Supplementary Video 1). Notably, the

number of mouth-opening actions increased along with 2MBA concentration (Fig. 1c, d).

Retching is physiologically characterized by activation of the diaphragm (inspiratory) and abdominal (expiratory) muscles⁶. To determine whether the mouth-opening actions triggered by 2MBA inhalation indeed represented retching-like behavior, we conducted electromyogram (EMG) recordings of the activities of these muscles during 2MBA exposure. The amplitude and frequency of the diaphragm and abdominal external oblique muscles activities both significantly increased during the mouth-opening actions, whereas this increase was absent during exposure to other unpleasant odorants (FEN, HEX, LIM, TMT, H₂S, and MgrB) or ddH₂O (Fig. 1e–g and Supplementary Figs. 1 and 2). We therefore refer to the phenotypic readout of our 2MBA paradigm as retching-like behavior.

As rancid odors have also been shown to induce psychological responses^{21,25}, we next investigated whether 2MBA exposure triggered an aversive response in mice. For this purpose, we conducted conditioned place aversion (CPA) tests, following previously described methods (Fig. 1h)^{26,27}. Heatmap analysis showed that mice spent less time in the 2MBA-paired chamber, resulting in a higher CPA score, compared to the ddH₂O-paired group (Fig. 1i, j). These data demonstrated that 2MBA could trigger aversion in mice.

To investigate whether the observed responses were triggered specifically through the olfactory system, we employed a previously described method for inducing anosmia²⁸ in which ZnSO₄ was bilaterally administered by intranasal irrigation for 5 successive days (Supplementary Fig. 3a). Exposure to 2MBA did not lead to retching-like behavior or aversion in the anosmia model mice as it did in saline-treated sham mice (Supplementary Fig. 3b–j). These results indicated that olfactory perception of spoiled food odor could induce defensive responses (retching-like behavior and aversion) in mice.

2MBA activates glutamatergic neurons in the anterior piriform cortex (aPir^{Glu}) to trigger retching-like behavior and aversion

The olfactory sensory neurons (OSNs) in the olfactory epithelium, responsible for perceiving odor molecules, are well-known to project to the olfactory bulb (OB)⁹. To identify brain regions downstream of the OB that are activated by 2MBA, we used FosCreER¹² (*Fos*^{TRAP2}) mice. Briefly, we injected an AAV expressing Cre-dependent FLP and an mCherry reporter (AAV2/I-DIO-FLP-mCherry) into the naris of *Fos*^{TRAP2} mice; we also injected an AAV expressing a FLP-dependent EGFP (AAV-fDIO-EGFP) into the OB. Three weeks after AAV injection, mice were intraperitoneally injected with the Cre-inducing agent, 4-hydroxytamoxifen (4-OHT)²⁹, then exposed to 2MBA using the same protocol as for the retching-like behavior paradigm (Fig. 2a and Supplementary Fig. 4a). This strategy enabled mCherry labeling of 2MBA-activated OSNs, with EGFP labeling of OB neurons innervated by 2MBA-activated OSNs. In whole brain sections, we could observe EGFP⁺ fibers positioned downstream of the EGFP-labeled OB neurons (Fig. 2b and Supplementary Fig. 4b). Examination of regions comprising the olfactory cortex, including the anterior piriform cortex (aPir) and posterior piriform cortex (pPir)³⁰, revealed that EGFP⁺ fibers were abundant in the aPir, but very scarce in other brain regions, including the well-known downstream of OB (pPir; olfactory tubercle, OT; or cortical amygdala, CoA) (Fig. 2c and Supplementary Fig. 4c–g). We therefore focused on the potential role of the aPir in 2MBA-triggered retching-like behavior and aversion.

To investigate whether aPir neurons participated in the olfactory response to 2MBA, we crossed *Fos*^{TRAP2} mice with *Ai14-tdTomato* mice, to enable tdTomato labeling in activated neurons expressing *Fos*, a marker of immediate-early neural activity, upon intraperitoneal injection of 4-OHT^{31,32}. We then monitored neuronal activation during 2MBA inhalation, as above, and found that tdTomato expression was significantly increased in the aPir compared to that ddH₂O-treated controls (Supplementary Fig. 5a, b). These results indicated that

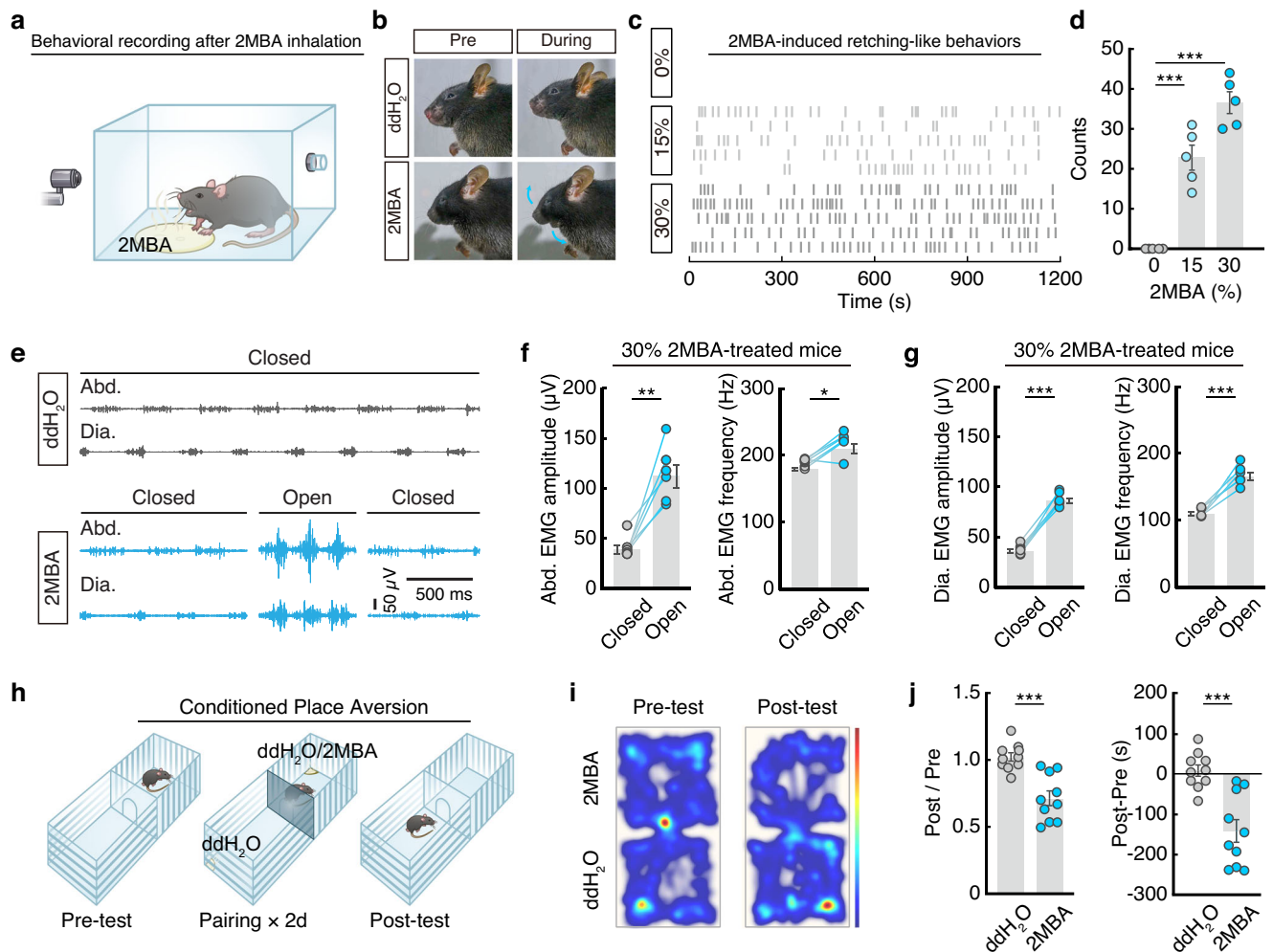


Fig. 1 | 2MBA-triggered retching-like behavior and aversion in mice. **a** Schematic of experimental paradigm for rancid odor-induced retching-like behavior using 2-methylbutyric acid (2MBA) evaporated in an enclosed space. **b–d** Representative images (**b**), example raster plots (**c**) and summarized data (**d**) of mouth-opening actions, *i.e.*, retching-like behavior, during exposure to 2MBA odor ($n = 5$ mice per group; $F_{2,12} = 6.257$, 0% vs. 15%, $P < 0.0001$; 0% vs. 30%, $P < 0.0001$). **e** EMG traces of the abdominal external oblique muscle (Abd.) and diaphragm muscle (Dia.) during mouth-opening actions. **f, g** Quantitation of EMG amplitude and frequency of Abd. (**f**) and Dia. (**g**) during mouth-opening actions ($n = 6$ mice per group; **f**, $P = 0.0024$ (left) and $P = 0.01$ (right); **g**, $P < 0.0001$ (left) and $P = 0.0006$ (right)). **h** Schematic of

experimental paradigm for rancid odor-induced conditioned place aversion (CPA) tests in ddH₂O-paired group and 2MBA-paired group. **i** Heatmaps for CPA tests in the 2MBA-paired group. **j** Summarized data for CPA tests in ddH₂O-paired group and 2MBA-paired group ($n = 10$ mice per group; $P = 0.0001$ (left) and $P = 0.0002$ (right)). Significance was assessed using two-tailed paired Student's *t* tests in panels (**f, g**), two-tailed unpaired Student's *t* tests in panel (**j**) one-way ANOVA with post hoc comparison between groups in panel (**d**). All data are presented as means \pm s.e.m. * $P < 0.05$, ** $P < 0.01$, *** $P < 0.001$. For detailed statistical information, see Supplementary Table 1. Source data are provided as a Source Data file.

olfactory exposure to 2MBA activated aPir neurons. As aPir neurons are known to comprise both glutamatergic and GABAergic neurons³³, we conducted immunofluorescence staining to determine which cell type was activated in the aPir. This analysis showed that 85.1% tdTomato signals colocalized with glutamate antibodies (Supplementary Fig. 5c, d). These results indicated that glutamatergic neurons in the aPir (aPir^{Glu}) respond to 2MBA.

We next explored the possibility that a specific subset of aPir^{Glu} neurons responds to 2MBA. For this purpose, we examined aPir^{Glu} neuronal responses to several odor stimuli (2MBA, FEN, HEX, LIM) at single-neuron resolution by injecting the aPir with an AAV expressing the Cre-dependent fluorescent Ca²⁺ indicator, GCaMP6m (AAV-DIO-GCaMP6m), and mounting a microendoscopic gradient index (GRIN) lens immediately above the aPir in *CaMK2-Cre* mice (Fig. 2d). We found that 30% of aPir neurons were activated by 2MBA inhalation alone, while 33.3% of neurons were activated by simultaneous exposure to 2MBA with other odors, and 36.7% of neurons exhibited no detectable response to 2MBA (Fig. 2e–g and Supplementary Fig. 6). To examine

the neural activity of these 2MBA-activated aPir^{Glu} neurons, we performed optical fiber photometry recordings in *Fos^{TRAP2}* mice. This assay revealed that the Ca²⁺ signal of 2MBA-activated aPir increased following inhalation of 2MBA, FEN, HEX, or LIM, but not ddH₂O, and the $\Delta F/F$ value was higher after 2MBA inhalation than after exposure to other odors (Fig. 2h–k). We also found that 2MBA-TRAPed neuronal activity increased in aPir in a concentration-dependent pattern, with inhalation of high 2MBA (30%) inducing greater $\Delta F/F$ values than low concentration (15%) (Supplementary Fig. 7a–c). These results were consistent with previous studies that also showed concentration-dependent responses to odors in Pir neurons^{33,34}. As these results collectively suggested that aPir^{Glu} neurons selectively respond to 2MBA inhalation, we subsequently focused on these 2MBA-activated aPir^{Glu} neurons.

We next investigated whether the 2MBA-activated aPir^{Glu} neurons were essential for 2MBA-triggered retching-like behavior and aversion. Given that aPir^{Glu} neuronal activity increased upon exposure to 2MBA, we selectively chemogenetically inhibited 2MBA-activated aPir^{Glu}

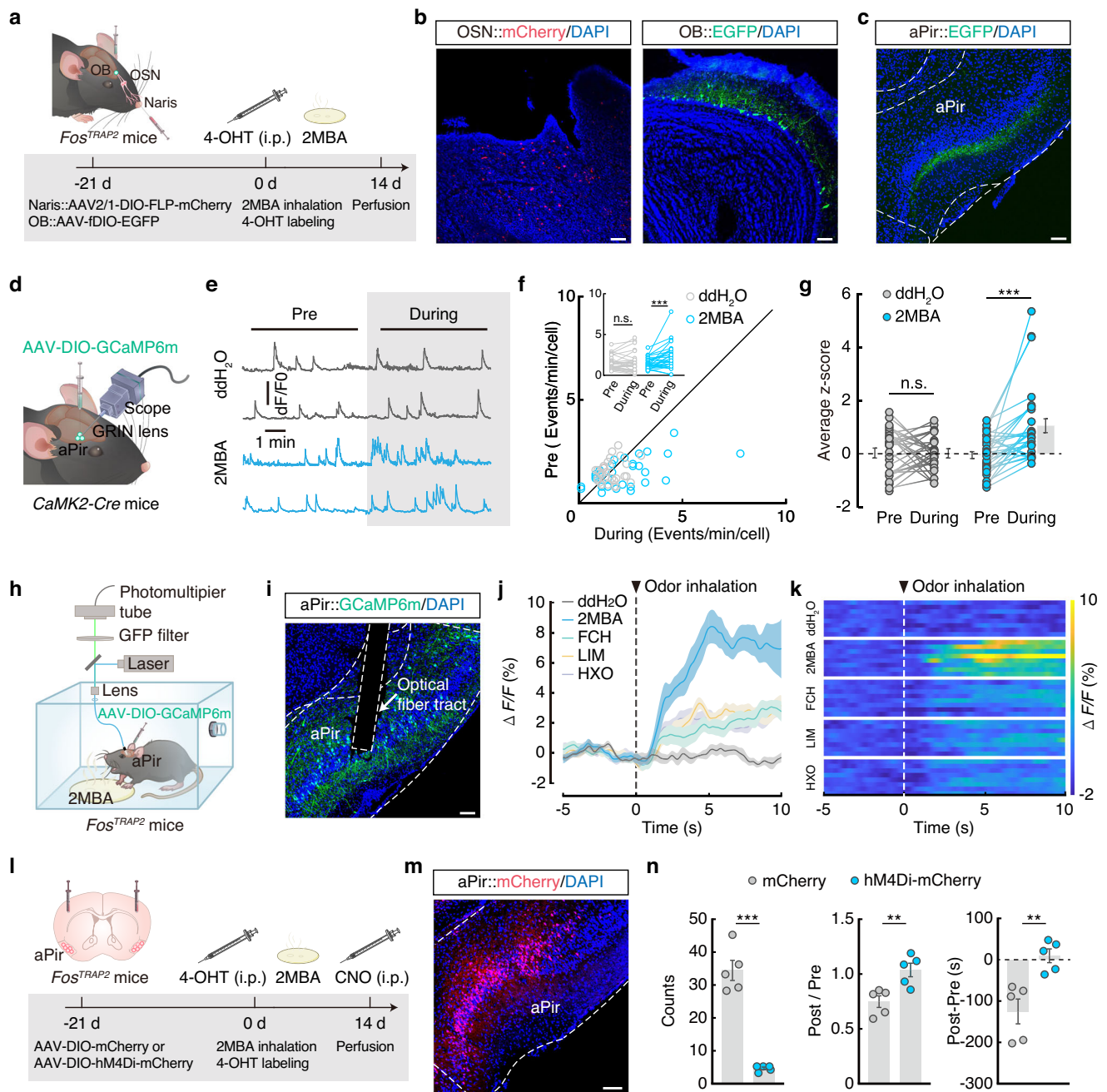


Fig. 2 | 2MBA activates aPir^{Glu} neuronal activity to trigger retching-like behavior and aversion. **a** Schematic for viral tracing in *Fos^{TRAP2}* mice. **b** Representative image of mCherry⁺ signals in the olfactory epithelium (left) and EGFP⁺ signals in the OB (right). Scale bars, 100 μ m. **c** Representative images of EGFP⁺ signals in the aPir. Scale bar, 100 μ m. **d** Schematic for in vivo microendoscopic imaging of aPir^{Glu} neurons in *CaMK2-Cre* mice. **e-g** Representative traces (e) and summarized data (f) of Ca²⁺ transient recordings, as well as the averaged z-score (g) of aPir^{Glu} neurons before and during 2MBA inhalation ($n = 30$ cells from 3 mice; f, $P = 0.0006$; g, $P < 0.0001$). **h** Schematic for in vivo fiber photometry recording of 2MBA-activated aPir neurons in *Fos^{TRAP2}* mice. **i** Representative image of AAV-DIO-GCaMP6m expression in the aPir. Scale bar, 100 μ m. **j, k** Average calcium activity (j) and heatmaps (k) of time-locked Ca²⁺ signals of GCaMP6m-expressing aPir neurons in response to 2MBA exposure ($n = 8$ mice). The dashed line indicates the onset of

odors exposure. **l** Schematic for chemogenetic inhibition of 2MBA-activated aPir neurons. **m** Representative image of mCherry⁺ signals in the aPir. Scale bar, 100 μ m. **n** Counts of retching-like behavior (left) and summarized data (middle and right) from CPA tests with inhibition of 2MBA-activated aPir neurons ($n = 5$ mice per group, $P < 0.0001$ (left), $P = 0.0075$ (middle), $P = 0.0057$ (right)). Significance was assessed using two-tailed unpaired Student's *t* tests in panel (n) and two-way ANOVA with post hoc comparison between groups in panels (f, g). All data are presented as means \pm s.e.m. ** $P < 0.01$, *** $P < 0.001$, n.s., not significant. For detailed statistical information, see Supplementary Table 1. OSN, olfactory sensory neurons; OB, olfactory bulb; aPir, anterior piriform cortex; FCH, (+)-fenchone; LIM, limonene; HXO, hexanol; 4-OHT, 4-hydroxytamoxifen; CNO, clozapine-N-oxide. Source data are provided as a Source Data file.

neuronal activity by injecting a Cre-dependent hM4Di-mCherry virus (AAV-DIO-hM4Di-mCherry) into the aPir of *Fos^{TRAP2}* mice. After 3 weeks, mice were intraperitoneally injected with 4-OHT, then exposed to 2MBA odor. Two weeks later, these mice were intraperitoneally

injected with the hM4Di-induction agent, clozapine-N-oxide (CNO), and evaluated for retching-like behavior and aversion (Fig. 2l, m). We observed that retching-like behavior (i.e., number of retching-like actions) and CPA scores were both significantly decreased in mice with

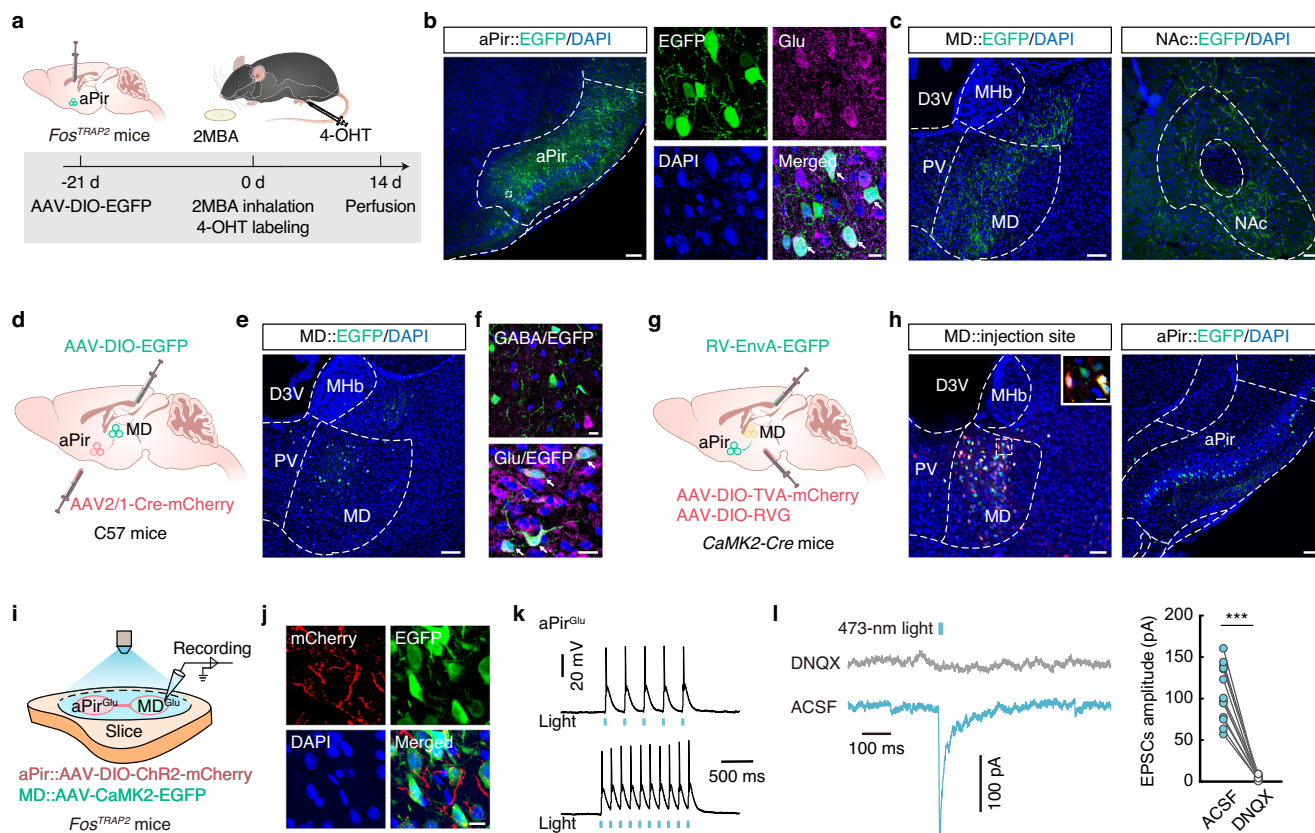


Fig. 3 | 2MBA-activated aPir^{Glu} neurons project to the mediodorsal thalamic nucleus (MD). **a** Schematic for virus injection to label activated aPir neurons in *Fos^{TRAP2}* mice. **b** Left: Representative image of EGFP⁺ signals in the aPir. Scale bar, 100 μ m. Right: Representative images of EGFP⁺ neurons colocalized with a glutamate-specific antibody. Scale bar, 10 μ m. **c** Representative images showing EGFP⁺ fibers in the MD and NAc. Scale bars, 100 μ m. **d** Schematic for virus injection of C57 mice. **e** Representative image showing EGFP⁺ signals in the MD. Scale bar, 100 μ m. **f** Representative images showing EGFP⁺ neurons colocalized with a glutamate-specific antibody, but not with a GABA-specific antibody. Scale bars, 20 μ m. **g** Schematic for virus injection of *CaMK2-Cre* mice. **h** Representative images of viral expression in the MD (left) and EGFP⁺ neurons in the aPir (right). Scale bars, 100 μ m. The inset depicts magnified view of the area in the white box. Scale bar, 20 μ m. **i** Schematic for virus injection and recording configuration in acute slices of

Fos^{TRAP2} mice. **j** Representative images of mCherry⁺ fibers in the MD surrounding EGFP⁺ neurons. Scale bar, 10 μ m. **k** Sample traces of action potentials evoked by light (blue line) recorded from mCherry⁺ neurons in acute brain slices containing aPir. **l** Representative traces (left) and summarized data (right) for light-evoked currents (blue bar) before and after treatment with the AMPA receptor antagonist, DNQX (10 μ M) ($n = 14$ cells from 10 mice, $P < 0.0001$). Significance was assessed using two-tailed paired Student's *t* tests in panel **l**. All data are presented as the mean \pm s.e.m. $^{***}P < 0.01$. For detailed statistical information, see Supplementary Table 1. MD mediodorsal thalamic nucleus, NAc nucleus accumbens, PV paraventricular thalamic nucleus, MHb medial habenular nucleus, D3V dorsal 3rd ventricle, ACSF artificial cerebrospinal fluid, DNQX 6,7-dinitroquinoxaline-2,3 (1H,4H)-dione. Source data are provided as a Source Data file.

inhibition of 2MBA-activated aPir^{Glu} neurons compared with mCherry-expressing controls (Fig. 2n). To confirm TRAP efficiency, mice were injected with the AAV-DIO-hM4Di-mCherry virus, then treated with 4-OHT induction and 2MBA odors prior to sacrifice (Supplementary Fig. 7d). Immunofluorescent staining for c-Fos in the aPir showed that 92.35% of tdTomato⁺ neurons colocalized with c-Fos⁺ nuclei, thus confirming the high efficiency of TRAP labeling in 2MBA-responsive neurons (Supplementary Fig. 7e, f). These results indicated that an increase in the aPir^{Glu} neuronal activity contributes to spoiled food odor-triggered retching-like behavior and aversion.

2MBA-activated aPir^{Glu} neurons project to the mediodorsal thalamic nucleus

To identify downstream neuronal targets of aPir^{Glu} neurons potentially involved in retching-like behavior and aversion triggered by 2MBA odor, we injected an AAV-DIO-EGFP into the aPir of *Fos^{TRAP2}* mice. Three weeks after AAV injection, mice were exposed to 2MBA odor following intraperitoneal injection of 4-OHT (Fig. 3a). Two weeks later, we observed EGFP⁺ neurons in the aPir (Fig. 3b) and EGFP⁺ fibers in several brain regions, including the mediodorsal thalamic nucleus (MD),

accumbens nucleus (NAc), lateral hypothalamic area (LH), and paratenial thalamic nucleus (PT) (Fig. 3c and Supplementary Fig. 8a, b).

To investigate whether these brain regions rich in EGFP⁺ fibers were also involved in the 2MBA-triggered responses, we monitored neuronal activity in these regions during exposure to 2MBA odor in *Fos^{TRAP2:Al14}* mice as above. We found that tdTomato expression was significantly increased in the MD (84% colocalized with a glutamate-specific antibody) and NAc (93% colocalized with a GABA-specific antibody), but not LH and PT, upon 2MBA exposure (Supplementary Fig. 8c–f). Given the relatively strong signals evoked by 2MBA, we focused on aPir^{Glu} \rightarrow MD and aPir^{Glu} \rightarrow NAc circuits in subsequent studies.

As the MD, composed of glutamatergic and GABAergic neurons, has been previously implicated in transmitting sensory information during pain and olfactory discrimination behaviors^{35,36}, we first sought to dissect the functional connectivity of the aPir \rightarrow MD circuit by anterograde monosynaptic tracing. To this end, we injected an AAV2/1-Cre-mCherry virus into the aPir and an AAV-DIO-EGFP virus into the MD (Fig. 3d). After 3 weeks, we observed EGFP⁺ neurons in the MD that colocalized with a glutamate-specific antibody rather than a GABA-

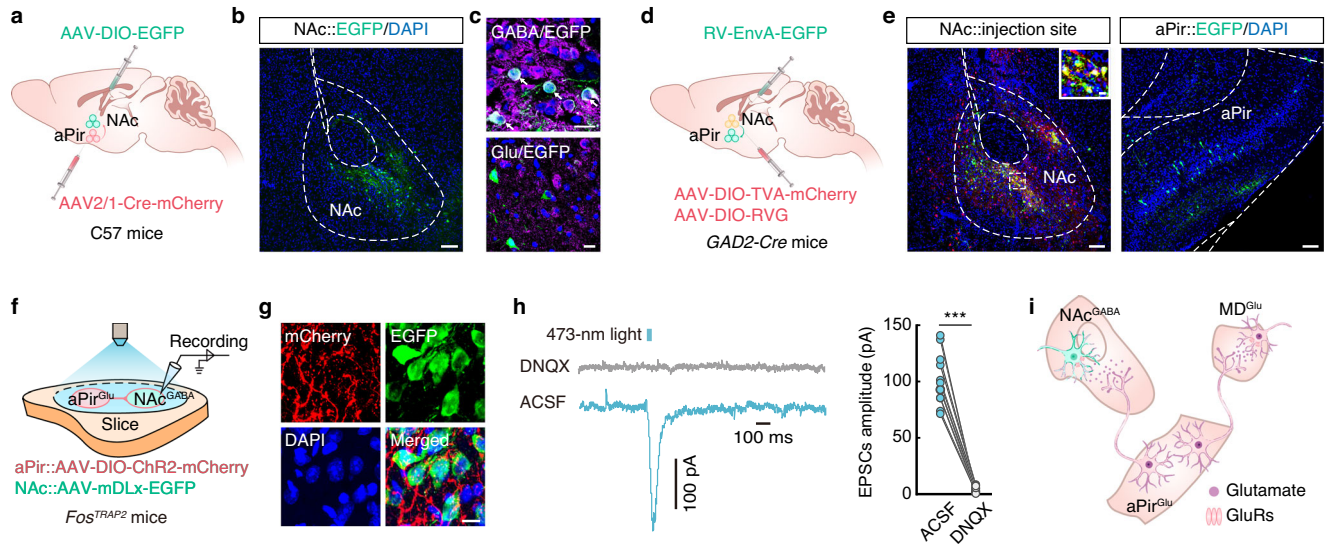


Fig. 4 | 2MBA-activated aPir^{Glu} neurons project to the NAc. **a** Schematic for virus injection of C57 mice. **b** Representative image of EGFP⁺ signals in the NAc. Scale bar, 100 μ m. **c** Representative images showing EGFP⁺ neurons colocalized with a GABA-specific antibody, but not with a glutamate-specific antibody. Scale bars, 20 μ m. **d** Schematic for virus injection of *GAD2-Cre* mice. **e** Representative images of virus expression in the NAc (left) and EGFP-labeled neurons in the aPir (right). Scale bars, 100 μ m. The inset depicts a magnified view of the area shown in the white box. Scale bar, 20 μ m. **f** Schematic for virus injection and the recording configuration in acute

slices of *Fos*^{TRAP2} mice. **g** Representative images showing mCherry⁺ fibers in the NAc surrounding EGFP⁺ neurons. Scale bar, 20 μ m. **h** Representative traces (left) and summarized data (right) for light-evoked currents (blue bar) before and after treatment with DNQX (10 μ M) ($n = 13$ cells from 10 mice, $P < 0.0001$). **i** A model for aPir^{Glu} \rightarrow MD and aPir^{Glu} \rightarrow NAc circuits. Significance was assessed using two-tailed paired Student's *t* tests in panel **h**. All data are presented as means \pm s.e.m. *** $P < 0.001$. For detailed statistical information, see Supplementary Table 1. NAc, accumbens nucleus. Source data are provided as a Source Data file.

specific antibody (Fig. 3e, f), indicating that aPir neurons projected to glutamatergic neurons in the MD (MD^{Glu}).

Next, to characterize the detailed organization of this aPir^{Glu} \rightarrow MD pathway, we used a cell-type-specific retrograde trans-monosynaptic tracing strategy in which helper viruses (AAV-EF1 α -DIO-TVA-mCherry and AAV-EF1 α -DIO-RVG) were injected into the MD of *CaMK2-Cre* mice. After 3 weeks, we injected a rabies virus (RV) EnvA-pseudotyped RV- Δ G-EGFP into the MD (Fig. 3g). At one week post RV injection, we detected EGFP⁺ neurons that co-localized with glutamate-specific antibody in the aPir (Fig. 3h and Supplementary Fig. 9). These data demonstrated that aPir^{Glu} neurons project to MD^{Glu} neurons.

We next examined functional connections of this aPir^{Glu} \rightarrow MD^{Glu} pathway by injecting an AAV-DIO-ChR2-mCherry into the aPir and an AAV-CaMK2-EGFP into the MD of *Fos*^{TRAP2} mice (Fig. 3i). At three weeks after injection, mice were exposed to 2MBA odor following intraperitoneal injection of 4-OHT. Two weeks later, mCherry⁺ fibers and EGFP⁺ neurons could be detected in the MD (Fig. 3j). Light stimulation of ChR2-containing terminals in the MD reliably triggered excitatory postsynaptic currents (EPSCs) in MD^{Glu} neurons, and this increase in EPSCs was eliminated upon treatment with 6,7-dinitroquinoxaline-2,3 (1*H*,4*H*)-dione (DNQX), an AMPA receptor antagonist (Fig. 3k, l). These findings suggested the presence of functional connections between 2MBA-activated aPir^{Glu} neurons and MD^{Glu} neurons.

2MBA-activated aPir^{Glu} neurons project to the NAc

Previous studies have shown that the NAc (95% of which comprises GABAergic neurons) is activated in odor-based discrimination tasks^{36,37}, indicating that it participates in olfactory processing. To explore the functional connectivity of this proposed aPir^{Glu} \rightarrow NAc circuit, we first injected an anterograde monosynaptic AAV2/1-Cre-mCherry into the aPir and an AAV-DIO-EGFP virus into the NAc of C57 mice (Fig. 4a). After 3 weeks, EGFP⁺ neurons that co-localized with a GABA-specific antibody rather than a glutamate-specific antibody could be observed in the NAc (Fig. 4b, c). In addition, Cre-dependent helper viruses (AAV-EF1 α -DIO-TVA-mCherry and AAV-EF1 α -DIO-RVG)

were injected into the NAc of *GAD2-Cre* mice, and 3 weeks later, RV- Δ G-EGFP was injected into the NAc (Fig. 4d). At one week post-RV injection, we identified EGFP⁺ neurons that colocalized with a glutamate-specific antibody in the aPir (Fig. 4e and Supplementary Fig. 10). These data suggested that aPir^{Glu} neurons also project to NAc^{GABA} neurons.

To then characterize functional connections of this aPir^{Glu} \rightarrow NAc^{GABA} circuit, we injected AAV-DIO-ChR2-mCherry into the aPir and AAV-mDLx-EGFP into the NAc of *Fos*^{TRAP2} mice (Fig. 4f). At three weeks after injection, mice were intraperitoneally injected with 4-OHT, then exposed to 2MBA odor. Two weeks later, mCherry⁺ fibers and EGFP⁺ neurons could be observed in the NAc (Fig. 4g). Light stimulation of ChR2-containing terminals in the NAc reliably triggered EPSCs in NAc^{GABA} neurons, which were subsequently abolished by DNQX treatment (Fig. 4h). These results thus confirmed the presence of functional connections from 2MBA-activated aPir^{Glu} neurons to NAc^{GABA} neurons.

To determine whether MD and NAc neurons received projections from the same aPir neuron, we injected retro-AAV-EGFP into the MD and retro-AAV-mCherry into the NAc of C57 mice (Supplementary Fig. 11a). We found that 75.44% of EGFP⁺ neurons in the aPir were not co-localized with mCherry⁺ neurons (Supplementary Fig. 11b–d). This suggested that distinct aPir neurons project to the MD and NAc, indicating that these aPir^{Glu}-innervated MD neurons and NAc neurons may mediate different behaviors induced by 2MBA. Taken together, these results showed that 2MBA-activated aPir^{Glu} neurons project to MD^{Glu} and NAc^{GABA} neurons (Fig. 4i).

The nose \rightarrow OB \rightarrow aPir \rightarrow MD circuit is essential for 2MBA-triggered retching-like behavior

To investigate the functional roles of the aPir^{Glu} \rightarrow MD^{Glu} and aPir^{Glu} \rightarrow NAc^{GABA} circuits in 2MBA-triggered retching-like behavior and aversion, we first conducted *in vivo* multi-tetrode electrophysiological recordings in the MD and NAc of freely moving mice (Fig. 5a and Supplementary Fig. 12a). Interestingly, time-locked recordings indicated that retching-like behavior triggered a significant increase in the

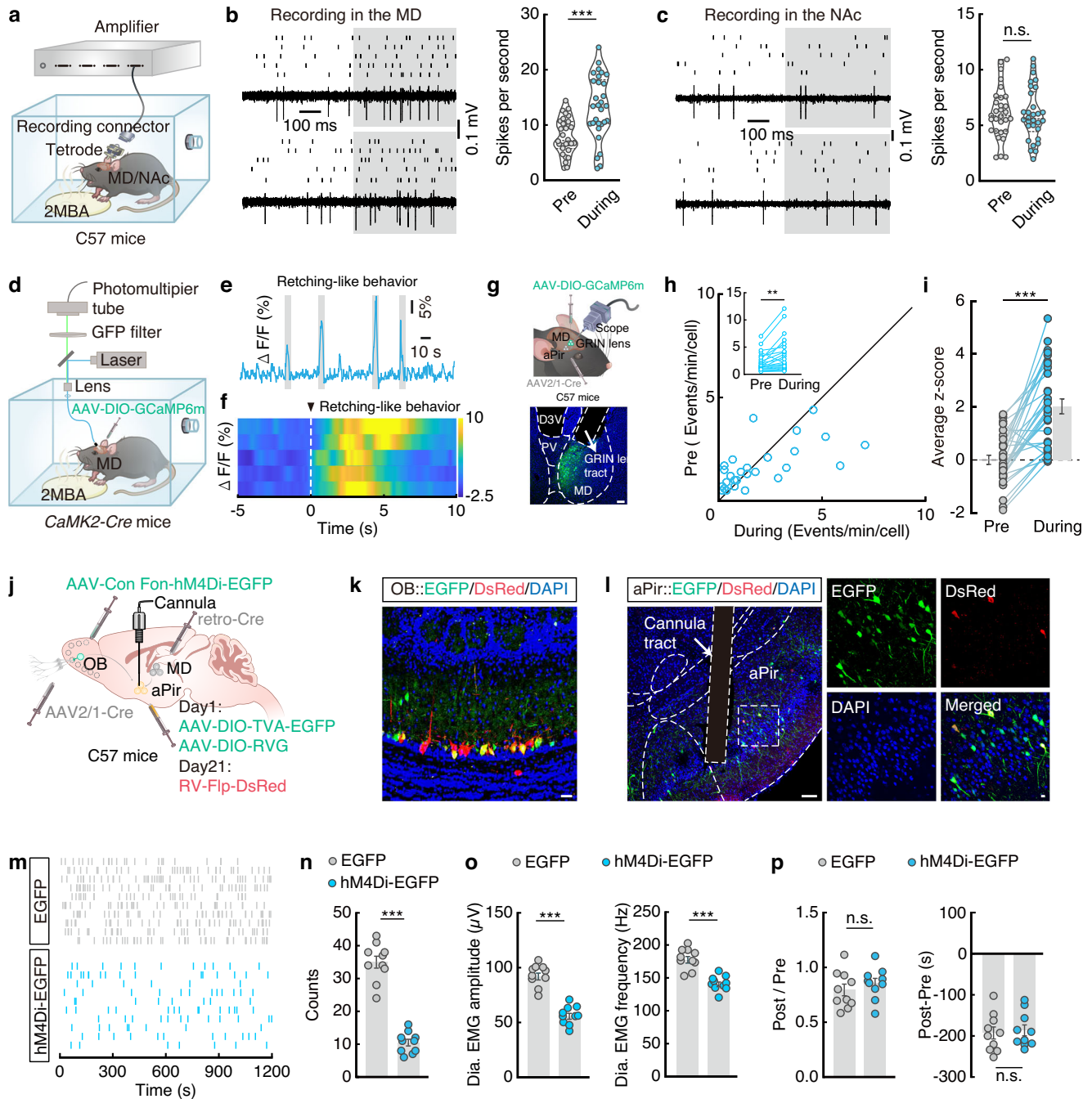


Fig. 5 | The nose → OB → aPir → MD circuit controls 2MBA-triggered retching-like behavior. **a** Schematic for in vivo multi-tetrode electrophysiological recording in the MD or NAc. **b** Representative traces (left) and summarized data (right) of firing rates in MD neurons before and during retching-like behavior ($n = 30$ cells from 5 mice, $P < 0.0001$). **c** Representative traces (left) and summarized data (right) of firing rates in NAc neurons before and during retching-like behavior ($n = 30$ cells from 5 mice). **d** Schematic for in vivo fiber photometry recording of MD^{CaMK2} neurons in *CaMK2-Cre* mice. **e, f** Representative trace (**e**) and heatmaps (**f**) of time-locked Ca^{2+} transient activity of 2MBA-triggered retching-like behavior. Gray bars in (**e**) indicate bouts of retching-like behavior. The dashed line in (**f**) indicates the onset of retching-like behavior ($n = 5$ mice). **g** Schematic (top) and representative image (bottom) for in vivo microendoscope imaging of aPir-innervated MD neurons in C57 mice. **h, i** Summarized data showing the events (**h**) and averaged z-score (**i**) of GCaMP6m-expressing MD neurons before and during retching-like behavior ($n = 30$ cells from 4 mice, **h**, $P = 0.0063$; **i**, $P < 0.0001$). **j** Schematic for optogenetic

inhibition of the nose → OB → aPir → MD circuit. **k** Representative image showing virus expression in the OB. Scale bar, 100 μ m. **l** Left: Representative image showing virus expression and cannula tract in the aPir. Scale bar, 100 μ m. Right: Typical images showing the DsRed-labeled neurons colocalized with EGFP⁺ signals in the aPir. Scale bar, 10 μ m. **m, n** Example raster plots (**m**) and counts (**n**) of retching-like behavior with inhibition of the nose → OB → aPir → MD circuit ($n = 10$ mice per group, $P < 0.0001$). **o** Summarized data of electromyography (EMG) recordings of diaphragm muscle with inhibition of the nose → OB → aPir → MD circuit ($n = 10$ mice per group, $P < 0.0001$ (left) and $P < 0.0001$ (right)). **p** Summarized data of CPA tests with inhibition of the nose → OB → aPir → MD circuit ($n = 10$ mice per group, $P = 0.3984$ (left) and $P = 0.7533$ (right)). Significance was assessed using two-tailed unpaired Student's *t* tests in panels (**n**–**p**), and two-tailed paired Student's *t* tests in panels (**b**, **c**, **h** and **i**). All data are presented as means \pm s.e.m. ****** $P < 0.01$, ******* $P < 0.001$, n.s., not significant. For detailed statistical information, see Supplementary Table 1. Source data are provided as a Source Data file.

firing rate of MD neurons, whereas no increase was observed in NAc neurons (Fig. 5b, c). Alternatively, we found that firing rate significantly increased in NAc neurons, but not MD neurons, when mice traveled from the 2MBA-unpaired chamber to the 2MBA-paired chamber in CPA post-tests (Supplementary Fig. 12b, c). Based on these firing patterns, we focused on the MD in 2MBA-triggered retching-like behavior and the NAc in 2MBA-triggered aversion.

To characterize the function of the aPir^{Glu}→MD^{Glu} circuit in 2MBA-triggered retching-like behavior, we used optical fiber photometry to monitor MD^{Glu} activity in freely moving *CaMK2-Cre* mice injected with an AAV-DIO-GCaMP6m in the MD following 2MBA exposure (Fig. 5d). Calcium signal recordings showed that 2MBA-induced retching-like behavior was associated with an obvious, time-locked increase in MD^{Glu} neuronal activity, while no such increase was observed upon travel from a 2MBA-unpaired chamber to a 2MBA-paired chamber in CPA post-tests (Fig. 5e, f and Supplementary Fig. 12d–f). To selectively monitor the response of aPir-innervated MD neurons at single-neuron resolution, we injected an AAV2/1-Cre into the aPir and an AAV-DIO-GCaMP6m into the MD of C57 mice carrying a GRIN lens mounted at the top of the MD (Fig. 5g). Consistent with the above results, 2MBA-triggered retching-like behavior was associated with time-locked increased calcium activity in aPir-innervated MD neurons, while no increase in calcium activity was observed during CPA post-tests (Fig. 5h, i and Supplementary Fig. 12g–i). A similar strategy was conducted in the mice exposed to TMT, H₂S or MgrB odors, we found no time-locked increased calcium activity in aPir-innervated MD neurons with odors exposure or CPA tests (Supplementary Fig. 12j–q). Together, these data indicate that MD neurons were specifically activated during 2MBA-triggered retching-like behavior.

To test whether increased activity in this aPir→MD circuit was required for 2MBA-triggered retching-like behavior, we chemogenetically inhibited the circuit through injection of the bilateral aPir with AAV-DIO-hM4Di-mCherry in *Fos^{TRAP2}* mice with cannulas implanted in the bilateral MD. After virus expression, CNO was administered to MD via intracranial microinjection (Supplementary Fig. 13a, b). We found that chemogenetic inhibition of the aPir→MD circuit alleviated the 2MBA-triggered retching-like behavior, but not aversion (Supplementary Fig. 13c). These results indicated that the aPir→MD circuit was essential for retching-like behavior, but not aversion, in response to 2MBA.

To assess whether activation of the aPir→MD circuit alone was sufficient to elicit retching-like behavior, we bilaterally injected AAV-DIO-ChR2-mCherry in the aPir and bilaterally implanted optical fibers in the MD of *Fos^{TRAP2}* mice (Supplementary Fig. 13d, e). We found that optical activation of the aPir→MD circuit could induce retching-like behavior in mice, but not aversion in real-time place aversion (RTPA) tests (Supplementary Fig. 13f). These cumulative results suggested that the aPir→MD circuit is necessary and sufficient to induce retching-like behavior akin to a rancid odor response.

To visualize the entire proposed nose→OB→aPir→MD circuit, we injected AAV2/1-Cre into the bilateral nares, AAV-Con Fon-hM4Di-EGFP into the bilateral OB, Cre-dependent helper viruses into the bilateral aPir, and retro-Cre into the bilateral MD. After 3 weeks of virus expression, RV-Flp-DsRed was injected into the bilateral aPir (Fig. 5j). At one week post-injection with RV, we observed neurons co-labeled with EGFP⁺ and DsRed⁺ in the OB (Fig. 5k), and thus visualized the entire proposed nose→OB→aPir→MD circuit.

To investigate whether this nose-to-brain axis was essential for 2MBA odor to trigger retching-like behavior and conditioned aversion, we used the same viral tracing strategy as above and bilaterally implanted cannulas in the aPir (Fig. 5l). Upon intracranial microinjection of CNO in the aPir to inhibit the nose→OB→aPir→MD circuit, we observed that retching-like behavior, but not conditioned aversion, was significantly reduced in response to 2MBA odor compared to that

in mCherry control mice (Fig. 5m–p). These results thus demonstrated that the nose→OB→aPir→MD circuit was required for 2MBA-triggered retching-like behavior, but not aversion.

The nose → OB → aPir → NAc circuit is essential for 2MBA-triggered aversion

To next investigate the role of the aPir^{Glu}→NAc^{GABA} circuit in mediating retching-like behavior and aversion to 2MBA odor, we conducted fiber photometry recordings of NAc^{GABA} activity in freely moving *GAD2-Cre* mice expressing AAV-DIO-GCaMP6m in the NAc (Fig. 6a). After three weeks of virus expression, time-locked recordings confirmed that calcium activity significantly increased when mice traveled from an unpaired chamber to a 2MBA-paired chamber in CPA post-tests, but did not increase during retching-like behavior (Fig. 6b, c and Supplementary Fig. 14a–c). To selectively monitor the response of aPir-innervated NAc neurons at single-neuron resolution, we injected the aPir with an AAV2/1-Cre and delivered an AAV-DIO-GCaMP6m virus to the NAc of C57 mice, then mounted a GRIN lens over the NAc (Fig. 6d). In line with our above findings, calcium activity showed a significant, time-locked increase upon entry into a 2MBA-paired chamber from an unpaired chamber in CPA post-tests, while no increase was observed during retching-like behavior (Fig. 6e–g and Supplementary Fig. 14d–f). Similar strategy was conducted in the mice exposed to TMT, H₂S or MgrB odors, we found time-locked increased calcium activity in aPir-innervated NAc neurons with odors exposure or entry into a TMT/H₂S/ MgrB-paired chamber in CPA post-tests (Supplementary Fig. 14g–n). Together, these data indicate that NAc neurons were activated during odor-triggered aversion.

In light of this increased aPir→NAc circuit activity in conditioned aversion to 2MBA, we selectively blocked this circuit by chemogenetic inhibition via bilateral aPir injection of AAV-DIO-hM4Di-mCherry in *Fos^{TRAP2}* mice and intracranial CNO administration through implanted cannulas in the bilateral NAc (Supplementary Fig. 15a, b), behavioral tests indicated that 2MBA-triggered aversion, but not retching-like behavior, was significantly decreased compared to that in mCherry controls (Supplementary Fig. 15c). These results indicated that the aPir→NAc circuit was required for aversion triggered by 2MBA odor.

To assess whether activation of the aPir→NAc circuit alone was sufficient to elicit aversion, we bilaterally injected AAV-DIO-ChR2-mCherry in the aPir and bilaterally implanted optical fibers in the NAc of *Fos^{TRAP2}* mice (Supplementary Fig. 15d, e). Optical activation of the aPir→NAc circuit in the absence of 2MBA odor induced aversion to a chamber coupled with the optical activation in RTPA tests, but did not result in observable retching-like behavior (Supplementary Fig. 15f). Together, these results suggested that the aPir→NAc circuit was necessary and sufficient to aversion, but not retching-like behavior.

To visualize the entire proposed nose→OB→aPir→NAc circuit, we bilaterally injected AAV2/1-Cre virus into the nares, AAV-Con Fon-hM4Di-EGFP into the bilateral OB, Cre-dependent helper viruses in the bilateral aPir, and retro-Cre virus into the bilateral NAc. After 3 weeks, we injected RV-Flp-DsRed into the bilateral aPir (Fig. 6h) and found EGFP⁺ DsRed⁺ neurons in the OB after one week of RV expression. These results thus depicted the anatomical connections of a nose→OB→aPir→NAc circuit (Fig. 6i).

To investigate whether this nose-to-brain axis was essential for the observed responses to 2MBA, we used the same viral tracing strategy as above and bilaterally implanted cannulas in the aPir (Fig. 6j). Behavioral assays following intracranial CNO application in the aPir to inhibit the nose→OB→aPir→NAc circuit showed that inhibiting this circuit alleviated conditioned aversion to 2MBA, but did not decrease 2MBA-triggered retching-like behavior (Fig. 6k–n). These results indicated that the nose→OB→aPir→NAc circuit was required for 2MBA-triggered aversion, but not retching-like behavior.

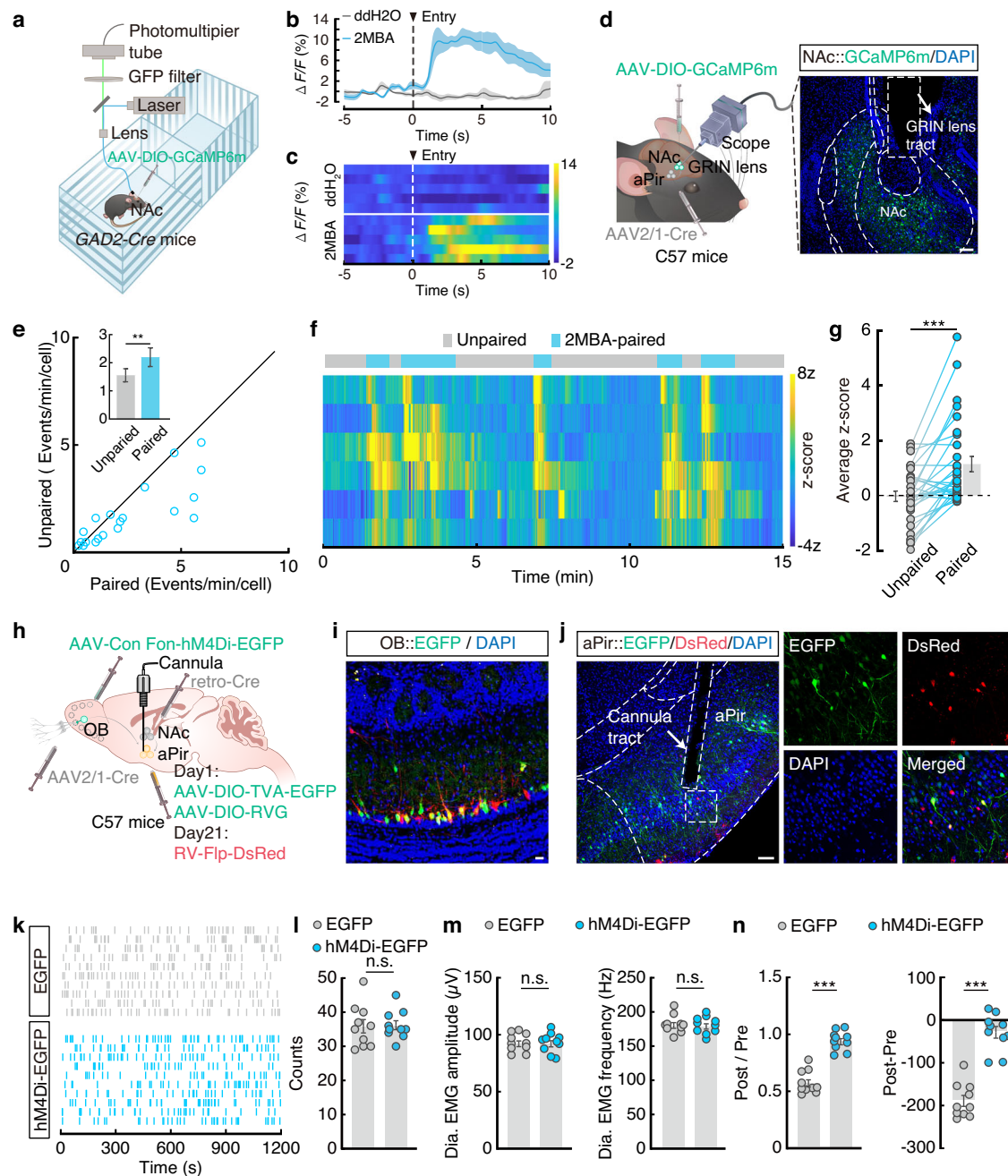


Fig. 6 | The nose → OB → aPir → NAc circuit controls 2MBA-triggered aversion. **a** Schematic for in vivo fiber photometry recording of NAc^{GABA} neurons in *GAD2-Cre* mice. **b, c** Representative trace (**b**) and heatmaps (**c**) of time-locked Ca²⁺ transient activity before and during entry into the 2MBA or ddH₂O-paired chamber ($n = 5$ mice per group). **d** Schematic (left) for in vivo microendoscope imaging of aPir-innervated NAc neurons in C57 mice; representative image (right) shows virus expression and Grin lens tract. Scale bar, 100 μ m. **e** Summarized data showing the events of GCaMP6m-expressing NAc neurons before and during C57 mice entering 2MBA-paired chamber ($n = 30$ cells from 5 mice, $P = 0.0023$). **f, g** Heatmaps (**f**, $n = 6$ cells from a representative mouse) and summarized data (**g**, $n = 30$ cells from 5 mice, $P < 0.0001$) showing the z-score of GCaMP6m-expressing NAc neurons before and during C57 mice entering the 2MBA-paired chamber. **h** Schematic for chemogenetic inhibition of the nose → OB → aPir → NAc circuit. **i** Representative image

showing virus expression in the OB. Scale bars, 100 μ m. **j** Left: Representative image showing virus expression and cannula tract in the aPir. Scale bar, 100 μ m. Right: Typical images showing the DsRed-labeled neurons colocalized with EGFP⁺ signals in the aPir. Scale bar, 10 μ m. **k, l** Example raster plots (**k**) and counts (**l**) of retching-like behavior with inhibition of the nose → OB → aPir → NAc circuit ($n = 10$ mice per group). **m** Summarized data of electromyography (EMG) recordings of diaphragm muscle with inhibition of the nose → OB → aPir → NAc circuit ($n = 10$ mice per group). **n** Summarized data (right) of CPA tests with inhibition of the nose → OB → aPir → NAc circuit ($n = 10$ mice per group, $P < 0.0001$ (left) and $P < 0.0001$ (right)). Significance was assessed using two-tailed unpaired Student's *t* tests in panels (**l**–**n**), and two-tailed paired Student's *t* tests in panels (**e** and **g**). All data are presented as means \pm s.e.m. ** $P < 0.01$, *** $P < 0.001$, n.s., not significant. For detailed statistical information, see Supplementary Table 1. Source data are provided as a Source Data file.

The nose-brain-muscle axis is essential for the retching-like behavior triggered by 2MBA

Given our observation that the nose → OB → aPir → MD circuit mediates 2MBA-triggered retching-like behavior and that retching behavior

involves increased activity of diaphragm and abdominal muscles, we next explored the possible basis through which the MD could modulate the activity of respiratory muscles. For this purpose, we injected a PRV-RFP virus into the abdominal external oblique muscle, and a PRV-

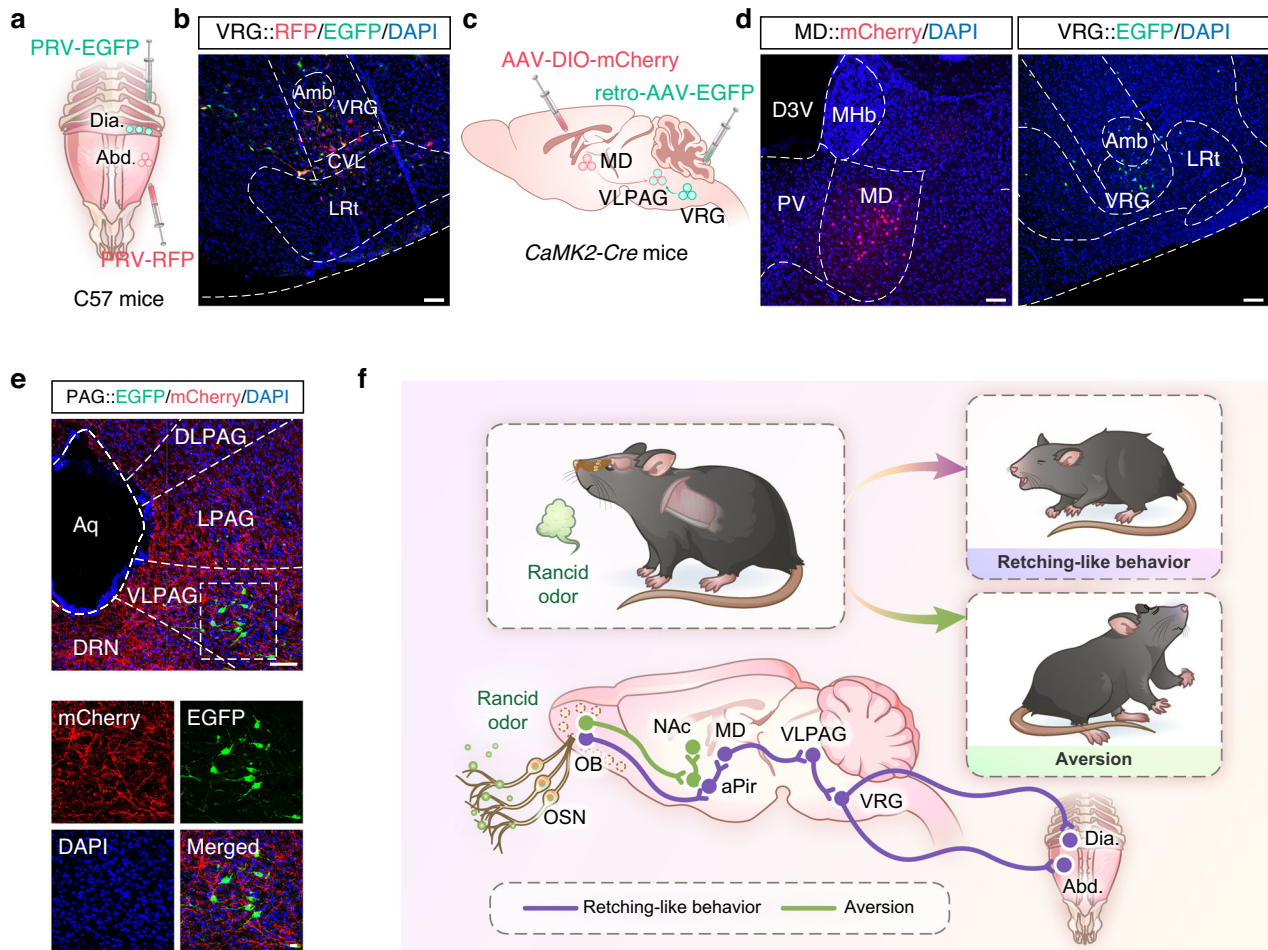


Fig. 7 | Defining a MD → VLPAG → VRG → respiratory muscles circuit. **a** Schematic for virus injection. **b** Representative image of neurons with co-localized EGFP⁺ and RFP⁺ signals in the VRG. Scale bar, 100 μ m. **c** Schematic for virus injection in *CaMK2-Cre* mice. **d** Representative images of virus expression in the MD (left) and VRG (right). Scale bars, 100 μ m. **e** Representative images of EGFP⁺ neurons surrounded by mCherry⁺ fibers in the VLPAG. Scale bars, 100 μ m (top) and 10 μ m (bottom). **f** Model of a nose-to-brain axis mediating 2MBA-triggered physiological retching

and psychological aversion. Amb ambiguous nucleus, VRG ventral respiratory group, LPGi lateral paragigantocellular nucleus, vsc ventral spinocerebellar tract, LRt lateral reticular nucleus, VLPAG ventrolateral periaqueductal gray, LPAG lateral periaqueductal gray, DLPAG dorsolateral periaqueductal gray, DRN dorsal raphe nucleus, Aq aqueduct; Abd abdominal external oblique muscle, Dia diaphragm muscle.

EGFP virus into the diaphragm muscle of C57 mice (Fig. 7a). Four days later, RFP⁺ EGFP⁺ co-labeled neurons were observed in several brain regions, including the PVN, raphe magnus nucleus, peritrigeminal zone, PAG, LH, and lateral reticular nucleus, as well as the ventral respiratory group (VRG), a region previously shown to contain respiratory neurons that coordinate muscle activity during retching³⁸ (Fig. 7b and Supplementary Fig. 16). To characterize connections between the MD and VRG in greater detail, we injected an AAV-DIO-mCherry and a retro-EGFP in the VRG. Three weeks later, we could detect EGFP⁺ neurons in the ventrolateral periaqueductal gray (VLPAG) surrounded by mCherry⁺ fibers (Fig. 7c–e). These results suggested that the MD likely regulates abdominal and diaphragm muscles through an MD → VLPAG → VRG circuit.

To determine whether activation of the MD → VLPAG circuit could trigger retching-like behavior, we injected an AAV-DIO-ChR2-mCherry into the MD and implanted optical fibers in the VLPAG of *CaMK2-Cre* mice. A 473 nm blue light was delivered to activate terminals in the VLPAG from MD^{Glu} neurons. We recorded retching-like behavior and EMG after optogenetic activation of the MD^{Glu} → VLPAG pathway. We found that optogenetic activation of this pathway induced increased retching-like behaviors and increased frequency and amplitude of abdominal external oblique muscle and diaphragmatic

muscle activity compared with mCherry control mice (Supplementary Fig. 17).

Taken together, these results demonstrated that distinct neural circuits participate in retching-like behavior (nose → OB → aPir → MD → VLPAG → VRG → respiratory muscles circuit) and aversion (nose → OB → aPir → NAc circuit) in response to rancid odor stimulus (Fig. 7f).

Discussion

This study defines two distinct circuits mediating defensive behaviors in response to odors associated with spoiled food. This multifunctional nose-to-brain axis provides a mechanism through which sensory-motor integration and interplay among the central and peripheral systems can stabilize metabolic function.

Many species depend on highly sensitive olfaction for survival³⁹. In mammals, the olfactory system plays essential roles in both survival and reproduction through perception of numerous volatile chemical cues that trigger innate behaviors (e.g., feeding, mating, freezing or escape)²¹. Unlike neuronal connectivity in other sensory modalities (e.g., vision, audition) that is organized into topographic maps that distinguish relevant features of a stimulus (e.g., spatial location, orientation, frequency), no apparent structure has been found in OB projections to the Pir, nor in intra-piriform connectivity⁴⁰.

This apparent lack of structure has made it difficult to decode the integration mechanism for olfactory information. Our results demonstrate that rancid odor activates aPir^{Glu} neurons, which in turn project to distinct brain regions responsible for mediating retching-like behavior and aversion. These findings thus establish a circuit pathway in the brain for transmitting and interpreting olfactory information to trigger subsequent physiological and psychological responses.

Mitral cells in the OB project to multiple regions, including the Pir, CoA and OT¹². Previous studies have revealed amygdala neurons encode odor valence, which preferentially respond to liked odors versus disliked odors^{41,42}. The OT has also been shown to contain spatially-segregated functional domains involved in distinct motivations or hedonic behaviors associated with olfaction^{43–45}. We found that 2MBA-TRAPed OB neurons predominantly innervate the aPir, rather than other brain regions. The specificity of such neural circuits may be related to the function of these nuclei. Findings in our current study demonstrated that the aPir is involved in retching-like behavior and aversion triggered by rancid odor.

The aPir encodes odorant information, perception, and odor-associated values, which is then communicated to other, high-order cortical areas, such as the prefrontal cortex, thereby supporting the establishment of odor associations with episodic-like or emotional memories^{14,15,46}. Anatomically, the aPir is well positioned to transform sensory representations into value representations that may subsequently lead to appropriate behavioral outputs, including defensive responses¹⁵. Our results showed that aPir projects to the MD to drive odor-triggered retching-like behaviors, or project to the NAC to drive odor-triggered aversion, indicating that aPir integrates olfactory information and serves as a hub linking odor sensory processing to behaviorally outputs.

Previous studies investigating vomiting and retching have focused on circuits in the central nervous system^{47,48}. Our results define a brain-muscle axis through which MD^{Glu} neurons project to the VLPAG, which in turn project to the VRG, and finally innervate abdominal and diaphragmatic muscles, thus providing a likely explanation for how the brain regulates muscle activity in humans. Our study thus advances current understanding of the whole-body neural bases underlying defensive responses.

Normal food odor has been shown to modulate lipid mobilization and insulin resistance in mice¹. Results in our current study indicate that spoiled food odors can activate MD^{Glu} and NAC^{GABA} neurons, inducing defensive responses (retching-like behavior and aversion) that facilitate voiding contamination from the digestive tract, or prevent its ingestion, to preserve metabolic homeostasis^{4,5}. Combined with a recent study of commensal microbes engineered to deliver drugs through a targeted nose-to-brain route⁴⁹, our study suggests a possible approach to developing odor-based therapies and intranasal neuromodulation strategies that help to maintain metabolic homeostasis and potentially treat metabolic disorders.

Although vomiting, retching and aversion serve as a protective mechanism for limiting consumption of toxins, or evacuating toxins after they have been ingested, these involuntary behaviors are also frequently reported side effects associated with obesity therapeutics (e.g., glucagon-like peptide-1 receptor agonists), and can strongly decrease treatment adherence^{50,51}. As traditional antiemetic medicine can induce adverse effects (e.g., headache, dizziness, drowsiness)⁵², non-pharmacological interventions for vomiting and retching may provide a valuable alternative therapeutic option. Our study shows that unpleasant odors can trigger retching through a nose-to-brain axis, thus illustrating a pathway through which some odors can regulate the activity of respiratory muscles. This afferent to efferent pathway provides a theoretical basis for the application of aromatherapies for suppressing vomiting or retching and warrants exploration for other involuntary responses to olfaction.

Methods

Animals

Male mice from the following strains were used in all experiments: C57BL/6J, *CaMK2-Cre*, *GAD2-Cre*, *FOS*^{2A-iCreER} (*Fos*^{TRAP2}), and *Aii4* (*RCL-tdT*). The mice, aged 8–10 weeks, were obtained from Charles River or Jackson Laboratories. They were housed in groups of five per cage under standard colony conditions, with ad libitum access to water and standard mouse chow. The animals were kept on a 12 h light/dark cycle (lights on from 8:00 AM to 8:00 PM) at a controlled temperature of 23–25 °C and 50% humidity. Deviations from these conditions occurred only during specific procedures, such as GRIN lens or tetrode array implantation. Mice were randomly assigned to experimental groups, and all procedures were approved by the Animal Care and Use Committee at the University of Science and Technology of China (USTC).

Retching-like behavior recording

Mice were placed in a transparent box (24 cm × 12 cm × 18 cm) and allowed to move freely. A piece of filter paper was positioned at the center of the box to facilitate the uniform evaporation of odorants. We pipetted 1 mL of odorants onto the filter paper, including ddH₂O, 2-methylbutyric acid (2MBA, 15% and 30%, corresponding to 1.375 × 10⁻³ mol and 2.75 × 10⁻³ mol, respectively), (+)-fenchone (FEN), hexanol (HEX), and limonene (LIM), trimethylthiazoline (TMT), NaHS (a H₂S-releasing agent), MgrB peptide. To record the behavior, we positioned a high-speed camera (160 frames/s) horizontally outside the box. The behavior was recorded continuously for 20 minutes.

Electromyogram (EMG) recording

EMG was recorded following previously described protocols in mice^{6,53}. Mice were anesthetized with isoflurane and maintained body temperature at 37 °C using a heating pad. To monitor muscle activity, EMG electrodes (A-M Systems, No. 793200) were implanted in the diaphragm and abdominal external oblique muscles, and fixed with UV glue. Subsequently, mice were head-fixed in a stereotaxic device (RWD). A ground electrode and a reference electrode were connected to the skull of mice. Connection cables of electrodes were attached firmly to the skull using tissue glue and dental cement. After surgery, the EMG signal was recorded, filtered (10–500 Hz), and digitized using a multi-channel signal acquisition apparatus (Medusa, Bio-Signal Technologies). A muscle was considered activated when the amplitude of the EMG signals increased by at least 30% above the basal level.

Conditioned position aversion (CPA) test

The CPA test was conducted using a custom-made two-chamber apparatus (50 cm × 25 cm × 25 cm) following previously reported protocols^{26,27}. A camera was mounted directly above the apparatus to track the movement of each mouse, and the data were analyzed using EthoVision XT 14 software (Noldus).

Pre-Phase (Day 1 and Day 2). Mice were gently introduced to the apparatus and allowed to explore both chambers freely for 15 min. The time spent in the preferred chamber on Day 2 served as the baseline.

Pairing-Phase (Day 3 and Day 4). For 2MBA-paired group mice, mice were confined to their preferred chamber and exposed to 2MBA for 30 min and were confined to the other chamber for 30 min paired with ddH₂O. For ddH₂O-paired group mice, mice were confined to their preferred chamber and exposed to ddH₂O for 30 min and were confined to the other chamber for 30 min paired with ddH₂O.

Post-Phase (Day 5). 24 hours after the final pairing phase, mice were allowed to freely explore both chambers of the apparatus for 15 min. The CPA score was calculated as the difference between the time spent in the preferred chamber during the post-test and the time spent in the

same chamber during the pre-test: CPA score = (time in the preferred chamber paired with 2MBA or ddH₂O)_{Post} - (time in the preferred chamber paired with 2MBA or ddH₂O)_{Pre}.

Real-time place aversion (RTPA) test

The same experimental apparatus used for CPA tests was employed for RTPA tests, following previously reported protocols^{26,27}. One day before RTPA testing, mice underwent a 15-minute pre-test. During this pre-test, they were placed at the center of the apparatus and allowed to freely explore both chambers. Mice that showed a strong preference for one side of the apparatus, spending more than 65% (> 585 s) or less than 35% (< 315 s) of the total exploration time on one side, were excluded from further testing. On the test day, we applied photostimulation in one randomly selected chamber (designated as the treatment-paired chamber), while the other chamber served as the no-stimulation (unpaired) chamber. Mice were placed in the center of the apparatus and allowed to explore freely for 20 min. Each entry into the treatment-paired chamber triggered photostimulation (473 nm, 5 ms pulses at 20 Hz) using a Master 8 pulse stimulator (A.M.P.I.). We recorded all stimulations and real-time travel trajectories using EthoVision XT 14 software (Noldus) for subsequent analysis. RTPA score = (time in the treatment-paired chamber)_{Test} - (time in the treatment-paired chamber)_{Pre}.

Anosmia induced by zinc sulfate (ZnSO₄) application

We induced the anosmia model by intranasally irrigating mice with ZnSO₄, following a previously described protocol²⁸. Mice were anesthetized with isoflurane, and 50 μ L of 5% ZnSO₄ was administered to each naris. This irrigation was repeated for 5 consecutive days. Sham mice received intranasal saline irrigation.

Immunohistochemistry

Mice were anesthetized with intraperitoneal pentobarbital sodium (20 mg/kg) and perfused with 0.9% (w/v) saline, followed by 4% (w/v) paraformaldehyde (PFA). After perfusion, the brains were extracted and fixed overnight in 4% PFA at 4 °C. The tissue was then incubated in 20% (w/v) and 30% (w/v) sucrose solutions at 4 °C until the brain tissue sank. We cut 40- μ m-thick coronal slices using a cryostat (Leica CMI860) for immunofluorescence. Following three washes with phosphate-buffered saline (PBS), the slices were blocked for 1 h at room temperature with a solution containing 5% bovine serum albumin (BSA) (w/v) and 0.5% Triton X-100 in PBS. Primary antibody incubation was conducted in a solution containing 3% BSA, 3% donkey serum, and 0.3% Triton X-100 in PBS for at least 24 hours at 4 °C. We used anti-glutamate (1:500, rabbit, Sigma), anti-GABA (1:500, rabbit, Sigma), and anti-c-Fos (1:500, rabbit, Synaptic Systems) as primary antibodies. Afterward, the slices were incubated with secondary antibodies conjugated to fluorophores (1:500, Invitrogen) for 1.5 h at room temperature. Finally, the slices were stained with 4,6-diamidino-2-phenylindole (DAPI; 1:2000, Sigma) for 6 min at room temperature. Fluorescence signals were observed and imaged using an FV3000 microscope.

Stereotaxic surgeries and viral injections

Mice were anesthetized with isoflurane (3% for induction; 1.5–2% for maintenance) and head-fixed in a stereotaxic device (RWD) on a heating pad to maintain body temperature. After shaving the fur, we made a small incision in the scalp to carefully expose the skull. Once exposed, we used a syringe equipped with a pulled glass microelectrode to ensure proper alignment of the skull in all planes. A small hole was drilled at the injection site, and the virus was injected at an infusion rate of 35 nl/min through the glass microelectrode, which was connected to an infusion pump (Micro 4, WPI). The pipette was left in place for 5 min post-injection to prevent backflow or spread of the virus.

For virus injection into the naris, mice were placed in a supine position on a heating blanket, with the mouth fixed. The glass microelectrode was inserted into the naris, and 1.5 μ L of either rAAV-Ef1 α -DIO-FLP-P2A-mCherry (AAV2/1-DIO-FLP-mCherry) or rAAV2/1-hSyn-Cre-pA (AAV2/1-Cre, 5.75 \times 10¹³ vg/ml) was injected.

For anterograde tracing of the aPir \rightarrow MD or aPir \rightarrow Nac projection, we injected rAAV-Ef1 α -Cre-P2A-mCherry (AAV2/1-Cre-mCherry, AAV2/1, 6.83 \times 10¹² vg/ml, 240 nl) into the aPir (ML: -2.90 mm, AP: +1.20 mm, DV: -4.24 mm). Subsequently, we injected rAAV-Ef1 α -DIO-EGFP-WPRE-pA (AAV-DIO-EGFP, AAV2/9, 1.95 \times 10¹² vg/ml, 200 nl) bilaterally into the MD (ML: -0.25 mm, AP: -0.46 mm, DV: -3.00 mm) or the Nac (ML: -1 mm, AP: +1.18 mm, DV: -4.00 mm). After waiting for 3 weeks to allow for viral expression, we perfused the mice and prepared brain slices to detect signals.

For retrograde tracing of the aPir \rightarrow MD or aPir \rightarrow Nac projections, we first injected a helper virus containing rAAV-Ef1 α -DIO-RVG-WPRE-pA (AAV-DIO-RVG, AAV2/9, 2 \times 10¹² vg/ml) and rAAV-Ef1 α -DIO-mCherry-F2A-TVA-WPRE-pA (AAV-DIO-TVA-mCherry, AAV2/9, 2 \times 10¹² vg/ml) at a 1:1 ratio (200 nl) into the MD or Nac unilaterally. After three weeks, we injected RV-CVS-ENVA-N2C(Δ G)-EGFP (2 \times 10⁸ IFU/ml, 200 nl) into the same location of the MD or Nac. Following a 7-day period for virus expression, we perfused the mice for subsequent experiments.

For retrograde tracing from the abdominal and diaphragm muscles, we injected 4 μ L of RFP-expressing pseudorabies virus (PRV-RFP; 2.00E + 09 PFU/ml) into the abdominal external oblique muscle and 4 μ L of EGFP-expressing pseudorabies virus (PRV-EGFP; 2.00E + 09 PFU/ml) into the diaphragm muscle. Seven days after injection, we perfused the mice to detect the PRV signal.

For retrograde tracing from the VRG, we injected AAV2/Retro-hSyn-EGFP (retro-AAV-EGFP, 5.08 \times 10¹² vg/ml, 200 nl) into the VRG (ML: -1.2 mm, AP: -7.67 mm, DV: -4.80 mm). Three weeks after injection, we perfused the mice to detect EGFP⁺ signal.

In vivo optogenetic manipulations

For optogenetic manipulation, we injected the Cre-dependent virus rAAV-Ef1 α -DIO-hChR2(H134R)-mCherry-WPRE-pA (AAV-DIO-ChR2-mCherry, AAV2/9, 1.63 \times 10¹³ vg/ml, 200 nl) into the aPir of *Fos*^{TRAP2} mice or into the MD of *CaMK2-Cre* mice. Following viral injection, we implanted optic fibers (200 μ m diameter, Newdoon) into the MD, Nac or VLPAG of anesthetized mice. To secure the optical fibers, we used tissue glue and dental cement to attach them firmly to the skull. Mice were allowed at least 3 weeks to recover before starting the experiments. To activate the circuits, we connected the optical fibers to a laser generator through fiber sleeves. A 473 nm blue light (2–5 mW, 20 Hz) using a Master-8 pulse stimulator (A.M.P.I.). Control mice received the Cre-dependent virus rAAV-Ef1 α -DIO-mCherry-WPRE-pA (AAV-DIO-mCherry, AAV2/9, 1.63 \times 10¹³ vg/ml, 200 nl) and underwent the same surgical procedure.

In vivo chemogenetic manipulations

For chemogenetic experiments, we injected the Cre-dependent virus rAAV-Ef1 α -DIO-hM4D(Gi)-mCherry-WPRE-pA (AAV-DIO-hM4D-mCherry, AAV2/9, 2.25 \times 10¹² vg/ml, 200 nl) into the aPir of *Fos*^{TRAP2} mice. Control mice received an injection of rAAV-Ef1 α -DIO-mCherry-WPRE-pA (AAV-DIO-mCherry, AAV2/9, 2.12 \times 10¹² vg/ml). For chemogenetic inhibition of 2MBA-activated aPir neurons, we administered CNO intraperitoneally. To inhibit the aPir \rightarrow MD and aPir \rightarrow Nac circuits, we implanted cannulas (internal diameter 0.25 mm, RWD) into the MD or Nac. CNO (3 μ M, 150 nL) was then microinjected through the cannulas⁵⁴.

In vivo optical fiber photometer recording

To record calcium signals, we injected the AAV-DIO-GCaMP6m virus and implanted an optic fiber (200 μ m diameter, Newdoon) into the

aPir of *Fos*^{TRAP2} mice, the MD of *CaMK2-Cre* mice, and the NAc of *GAD2-Cre* mice. Recordings were conducted three weeks after viral expression. A mono fiber optic patch cord was connected to the fiber photometry system (Inper) and secured to the implanted fiber using a ceramic sleeve and black heat-shrinkable tubing. A 470 nm LED light (3 ms pulses, 40 Hz) was bandpass-filtered (470/10 nm) and delivered to the fiber tip to excite GCaMP6m fluorescence. The emitted fluorescence was captured at 40 fps using InperSignal. A 410-nm LED light, bandpass-filtered (410/10 nm), served as the isosbestic control channel. Fluorescence changes ($\Delta F/F$) were calculated using the formula $\Delta F/F (\%) = [(F(\text{duration}) - F(\text{baseline})) / F(\text{baseline})] \times 100\%$ ⁵⁵. GCaMP6m fluorescence intensity was recorded while mice were exposed to odor stimuli, with signals recorded 5 seconds before the odor presentation used as the baseline. Fluorescence was also measured during retching-like behavior and CPA tests, with baseline signals defined as those recorded 5 seconds prior to retching or traveling in odor-paired chambers. Heatmaps and averaged calcium traces were generated using InperPlot software (Inper Technology, Hangzhou).

In vivo electrophysiological recordings

Mice were housed individually before the implantation of tetrode arrays. Following a 3-day adaptation period, we implanted custom-made movable tetrode arrays with screw-driven microdrives and four implantable tetrodes into the MD or NAc. After surgery, mice were given a recovery period of at least 3 days. During this time, electrodes attached to their heads were connected to cables for daily 20 min adaptation sessions. During recordings, mice were placed in behavioral boxes surrounded by copper mesh and allowed to move freely. Neuronal signals were amplified, filtered (300–5000 Hz bandwidth), and stored using Neurostudio software. Offline analyses were performed with Neuroexplorer 4 (Nex Technologies) and Offline Sorter 4 (Plexon).

In vitro electrophysiological recordings

Brain slice preparation. Mice were deeply anesthetized using isoflurane. After anesthesia, we performed intracardiac perfusion with ice-cold, oxygenated artificial cerebrospinal fluid (NMDG ACSF; osmolarity: 300–305 mOsm/kg, pH: 7.3–7.4). The NMDG ACSF consisted of the following components (in mM): 93 NMDG, 2.5 KCl, 25 glucose, 0.5 CaCl₂, 5 Na-ascorbate, 20 HEPES, 3 Na-pyruvate, 1.2 NaH₂PO₄, 3 glutathione, 30 NaHCO₃, 10 MgSO₄, and 2 thiourea. We cut coronal slices (300 μ m) containing the MD or NAc using a vibrating microtome (VT1200s, Leica, Germany). The slices were then transferred to HEPES ACSF solution for at least 1 hour. This HEPES ACSF solution (28 °C, osmolarity: 300–305 mOsm/kg, pH 7.3–7.4) contained (in mM): 2.5 KCl, 3 glutathione (GSH), 92 NaCl, 3 sodium pyruvate, 1.2 NaH₂PO₄, 2 MgSO₄, 2 thiourea, 30 NaHCO₃, 25 glucose, 20 HEPES, 5 Na-ascorbate, and 2 CaCl₂. After incubation, we placed the brain slices in a recording chamber (Warner Instruments, USA) for whole-cell recordings. The slices were continuously perfused with standard ACSF (32 °C, osmolarity: 300–310 mOsm/kg, pH: 7.3–7.4). This ACSF contained (in mM): 3 HEPES, 10 glucose, 129 NaCl, 3 KCl, 2.4 CaCl₂, 1.3 MgSO₄, 1.2 KH₂PO₄, and 20 NaHCO₃, at a flow rate of 3 ml/min.

Light-evoked response. We visualized neurons in the MD and NAc brain regions using a 40 \times water immersion objective on an upright microscope (BX51WI, Olympus, Japan). Patch pipettes were fabricated by horizontally pulling and fire-polishing borosilicate glass capillary tubes to achieve a tip resistance of 5–7 M Ω . These pipettes were filled with a potassium gluconate-based internal solution. An optical fiber (200 μ m in diameter) was positioned 0.2 mm above the brain slice and aligned with the target neurons to deliver blue laser light. To confirm the functionality of the AAV-DIO-ChR2-mCherry virus, we visualized neurons expressing ChR2-mCherry in the aPir and stimulated them with blue laser light (473 nm, 5–10 mW) at pulse widths of 15 ms and

frequencies of 5 Hz or 10 Hz. Following blue laser light stimulation of ChR2-mCherry-expressing aPir neuronal fibers in MD or NAc brain slices, we recorded excitatory postsynaptic currents (EPSCs) in voltage-clamp mode at a holding potential of –70 mV.

Microendoscope imaging and data processing

For microendoscope imaging, we delivered the Cre-dependent virus rAAV-Ef1 α -DIO-GCaMP6m-WPRE-pA (AAV-DIO-GCaMP6m, AAV2/9, 1.63 $\times 10^{13}$ vg/ml) separately into the aPir, MD, and NAc. The injection pipette was left in place for 20 min following virus delivery to ensure proper diffusion. Subsequently, we implanted microendoscopic gradient index (GRIN) lenses (6.1 mm in length, 0.5 mm in diameter; or 4.00 mm in length, 1.0 mm in diameter, Inscopix, USA) into the aPir, MD, and NAc of anesthetized mice. The GRIN lenses implanted in the MD were modified as described^{56–58}.

After 21 days of surgical recovery, we attached an integrated miniature fluorescence microscope (Inscopix, USA) to the baseplate on the mice's heads. To ensure adaptation, the mice underwent 15 min sessions of habituation for 3 consecutive days before the recording sessions. During data acquisition, we recorded image data at 20 Hz per session. The collected image data were processed offline using Inscopix Data Processing Software (version 1.1.6, Inscopix, USA), following previously established protocols^{56–58}.

Statistical analysis

We performed statistical comparisons between two groups using paired or unpaired two-tailed Student's *t* tests. For multiple-group comparisons, we applied one-way or two-way ANOVA followed by post hoc analyses. Statistical significance was defined as follows: **P* < 0.05, ***P* < 0.01, and ****P* < 0.001. Results are presented as means \pm s.e.m. Statistical analysis and graphing were conducted using OriginPro 2023 (Origin Lab, USA) and GraphPad Prism 8 (GraphPad Software, USA). Offline analysis of in vitro electrophysiological data was performed using Clampfit software (version 10.7, Axon Instruments, USA). For in vivo electrophysiological data, we used NeuroExplorer (Plexon, USA). Microendoscopic imaging data were analyzed offline using Inscopix Data Processing Software (version 1.1.6, Inscopix, USA). All images were created by the authors using Adobe Illustrator.

Reporting summary

Further information on research design is available in the Nature Portfolio Reporting Summary linked to this article.

Data availability

All data necessary to understand and assess the conclusions of this study are available in the main text or the supplementary materials. There are no restrictions on data availability in the manuscript. Source data are provided in this paper.

References

1. Tsuneki, H. et al. Food odor perception promotes systemic lipid utilization. *Nat. Metab.* **4**, 1514–1531 (2022).
2. Brandt, C. et al. Food perception primes hepatic ER homeostasis via melanocortin-dependent control of mTOR activation. *Cell* **175**, 1321–1335 (2018).
3. Mutlu, A. S., Gao, S. M., Zhang, H. & Wang, M. C. Olfactory specificity regulates lipid metabolism through neuroendocrine signaling in *Caenorhabditis elegans*. *Nat. Commun.* **11**, 1450 (2020).
4. Tizard, I. & Skow, L. The olfactory system: the remote-sensing arm of the immune system. *Anim. Health Res. Rev.* **22**, 14–25 (2021).
5. Gordon, A. R. et al. Human scent as a first-line defense against disease. *Sci. Rep.* **13**, 16709 (2023).
6. Xie, Z. et al. The gut-to-brain axis for toxin-induced defensive responses. *Cell* **185**, 4298–4316 (2022).

7. Reinke, H. & Asher, G. Circadian clock control of liver metabolic functions. *Gastroenterology* **150**, 574–580 (2016).
8. Wagner, M. et al. CAR and PXR agonists stimulate hepatic bile acid and bilirubin detoxification and elimination pathways in mice. *Hepatology* **42**, 420–430 (2005).
9. Chen, P. et al. Olfactory sensory experience regulates gliomagenesis via neuronal IGF1. *Nature* **606**, 550–556 (2022).
10. Mombaerts, P. et al. Visualizing an olfactory sensory map. *Cell* **87**, 675–686 (1996).
11. Blazing, R. M. & Franks, K. M. Odor coding in piriform cortex: mechanistic insights into distributed coding. *Curr. Opin. Neurobiol.* **64**, 96–102 (2020).
12. Liberles, S. D. Mammalian pheromones. *Annu. Rev. Physiol.* **76**, 151–175 (2014).
13. Matsukawa, M., Yoshikawa, M., Katsuyama, N., Aizawa, S. & Sato, T. The anterior piriform cortex and predator odor responses: modulation by inhibitory circuits. *Front. Behav. Neurosci.* **16**, 896525 (2022).
14. Choi, G. B. et al. Driving opposing behaviors with ensembles of piriform neurons. *Cell* **146**, 1004–1015 (2011).
15. Wang, P. Y. et al. Transient and persistent representations of odor value in prefrontal cortex. *Neuron* **108**, 209–224 e206 (2020).
16. Fukuda, H. & Koga, T. The Botzinger complex as the pattern generator for retching and vomiting in the dog. *Neurosci. Res.* **12**, 471–485 (1991).
17. Rabin, B. M. & Hunt, W. A. Relationship between vomiting and taste aversion learning in the ferret: studies with ionizing radiation, lithium chloride, and amphetamine. *Behav. Neural Biol.* **58**, 83–93 (1992).
18. Miller, A. D. & Ruggiero, D. A. Emetic reflex arc revealed by expression of the immediate-early gene c-fos in the cat. *J. Neurosci.* **14**, 871–888 (1994).
19. Huo, L. et al. Brain circuits for retching-like behavior. *Natl. Sci. Rev.* **11**, nwad256 (2024).
20. Kobayakawa, K. et al. Innate versus learned odour processing in the mouse olfactory bulb. *Nature* **450**, 503–508 (2007).
21. Saraiva, L. R. et al. Combinatorial effects of odorants on mouse behavior. *Proc. Natl. Acad. Sci. USA* **113**, E3300–E3306 (2016).
22. Wang, H. et al. A molecularly defined amygdala-independent tetrasynaptic forebrain-to-hindbrain pathway for odor-driven innate fear and anxiety. *Nat. Neurosci.* **27**, 514–526 (2024).
23. Koike, K. et al. Danger perception and stress response through an olfactory sensor for the bacterial metabolite hydrogen sulfide. *Neuron* **109**, 2469–2484 (2021).
24. Bufe, B. et al. Bacterial MgrB peptide activates chemoreceptor Fpr3 in mouse accessory olfactory system and drives avoidance behaviour. *Nat. Commun.* **10**, 4889 (2019).
25. De-Souza, E. A., Thompson, M. A. & Taylor, R. C. Olfactory chemosensation extends lifespan through TGF-beta signaling and UPR activation. *Nat. Aging* **3**, 938–947 (2023).
26. Tian, Z. et al. The interhemispheric amygdala-accumbens circuit encodes negative valence in mice. *Science* **386**, eadp7520 (2024).
27. Dong, Y. et al. Stress relief as a natural resilience mechanism against depression-like behaviors. *Neuron* **111**, 3789–3801 (2023).
28. Fang, S. et al. Sexually dimorphic control of affective state processing and empathic behaviors. *Neuron* **112**, 1498–1517 (2024).
29. Su, Y. et al. Brainstem Dbh(+) neurons control allergen-induced airway hyperreactivity. *Nature* **631**, 601–609 (2024).
30. Cai, L., Argunsah, A. O., Damiou, A. & Karayannis, T. A nasal chemosensation-dependent critical window for somatosensory development. *Science* **384**, 652–660 (2024).
31. Allen, W. E. et al. Thirst-associated preoptic neurons encode an aversive motivational drive. *Science* **357**, 1149–1155 (2017).
32. Guenther, C. J., Miyamichi, K., Yang, H. H., Heller, H. C. & Luo, L. Permanent genetic access to transiently active neurons via TRAP: targeted recombination in active populations. *Neuron* **78**, 773–784 (2013).
33. Yang, Y. et al. A neural circuit for lavender-essential-oil-induced antinociception. *Cell Rep.* **43**, 114800 (2024).
34. Bolding, K. A. & Franks, K. M. Recurrent cortical circuits implement concentration-invariant odor coding. *Science* **361**, <https://doi.org/10.1126/science.aat6904> (2018).
35. Fredericksen, K. E., McQueen, K. A. & Samuelsen, C. L. Experience-dependent c-Fos expression in the mediodorsal thalamus varies with chemosensory modality. *Chem. Senses* **44**, 41–49 (2019).
36. Slotnick, B. M. & Kaneko, N. Role of mediodorsal thalamic nucleus in olfactory discrimination learning in rats. *Science* **214**, 91–92 (1981).
37. Gmaz, J. M. & van der Meer, M. A. A. Context coding in the mouse nucleus accumbens modulates motivationally relevant information. *PLoS Biol.* **20**, e3001338 (2022).
38. Horn, C. C. In *Nausea and Vomiting: Diagnosis and Treatment* (eds Kenneth L. K. & William L. H.) 15–25 (Springer International Publishing, 2017).
39. Dewan, A., Pacifico, R., Zhan, R., Rinberg, D. & Bozza, T. Non-redundant coding of aversive odours in the main olfactory pathway. *Nature* **497**, 486–489 (2013).
40. Chen, Y. et al. High-throughput sequencing of single neuron projections reveals spatial organization in the olfactory cortex. *Cell* **185**, 4117–4134 (2022).
41. Kehl, M. S. et al. Single-neuron representations of odours in the human brain. *Nature* **634**, 626–634 (2024).
42. Pignatelli, M. & Beyeler, A. Valence coding in amygdala circuits. *Curr. Opin. Behav. Sci.* **26**, 97–106 (2019).
43. Yamaguchi, M. Connectivity of the olfactory tubercle: inputs, outputs, and their plasticity. *Front. Neural Circuits* **18**, 1423505 (2024).
44. Yamaguchi, M. Functional sub-circuits of the olfactory system viewed from the olfactory bulb and the olfactory tubercle. *Front. Neuroanat.* **11**, 33 (2017).
45. Wang, W. et al. A midbrain-to-ventral-striatum dopaminergic pathway orchestrates odor-guided insect predation in mice. *Proc. Natl. Acad. Sci. USA* **122**, e2514847122 (2025).
46. Silvas-Baltazar, M., Lopez-Oropeza, G., Duran, P. & Martinez-Canabal, A. Olfactory neurogenesis and its role in fear memory modulation. *Front. Behav. Neurosci.* **17**, 1278324 (2023).
47. Catenoix, H. et al. The role of the anterior insular cortex in ictal vomiting: a stereotactic electroencephalography study. *Epilepsy. Behav.* **13**, 560–563 (2008).
48. Scalera, G. Effects of conditioned food aversions on nutritional behavior in humans. *Nutr. Neurosci.* **5**, 159–188 (2002).
49. Shen, H. et al. Engineered commensals for targeted nose-to-brain drug delivery. *Cell* **188**, 1545–1562 (2025).
50. Huang, K. P. et al. Dissociable hindbrain GLP1R circuits for satiety and aversion. *Nature* **632**, 585–593 (2024).
51. Wadden, T. A. et al. Effect of subcutaneous semaglutide vs placebo as an adjunct to intensive behavioral therapy on body weight in adults with overweight or obesity: the STEP 3 randomized clinical trial. *JAMA* **325**, 1403–1413 (2021).
52. Elvir-Lazo, O. L., White, P. F., Yumul, R. & Cruz Eng, H. Management strategies for the treatment and prevention of postoperative/post-discharge nausea and vomiting: an updated review. *F1000Res.* **9**, <https://doi.org/10.12688/f1000research.21832.1> (2020).
53. Xie, Z. et al. Mechanically evoked defensive attack is controlled by GABAergic neurons in the anterior hypothalamic nucleus. *Nat. Neurosci.* **25**, 72–85 (2022).
54. Tang, H. D. et al. A neural circuit for the suppression of feeding under persistent pain. *Nat. Metab.* **4**, 1746–1755 (2022).
55. Zhu, X. et al. Distinct thalamocortical circuits underlie allodynia induced by tissue injury and by depression-like states. *Nat. Neurosci.* **24**, 542–553 (2021).

56. Gong, R., Xu, S., Hermundstad, A., Yu, Y. & Sternson, S. M. Hindbrain double-negative feedback mediates palatability-guided food and water consumption. *Cell* **182**, 1589–1605 (2020).
57. Dong, W. Y. et al. Brain regulation of gastric dysfunction induced by stress. *Nat. Metab.* **5**, 1494–1505 (2023).
58. Zhu, X. et al. Somatosensory cortex and central amygdala regulate neuropathic pain-mediated peripheral immune response via vagal projections to the spleen. *Nat. Neurosci.* **27**, 471–483 (2024).

Acknowledgements

This work was supported by the Plans for Major Provincial Science & Technology Projects (202303a07020002 to Z.Z.), the National Key Research and Development Program of China (STI2030-Major Projects 2021ZD0203100 to Z.Z.), the National Natural Science Foundation of China (grants 32025017 to Z.Z., 32530043 to Z.Z., 32241013 to Z.Z., 32422035 to X.Z., 32371045 to X.Z., 32541070 to X.Z., 32121002 to Z.Z., 323B2031 to W.D., 32500882 to W.D., 32471182 to H.W., 32271176 to W.W., 81971264 to W.W., 82471162 to W.Z.), the China National Post-doctoral Program for Innovative Talents (BX20240346 to W.D.), the Research Funds of Center for Advanced Interdisciplinary Science and Biomedicine of the Institute of Health and Medicine (QYZD20220007 to Z.Z.), the USTC Research Funds of the Double First-Class Initiative (YD9100002064 to Z.Z., YD9100002041 to X.Z., YD9100002085 to W.W., YD9100002510 to W.D.), and Zhang Zhi Expert Workstation, Yunnan Provincial Department of Science and Technology (202405AF140117 to Z.Z.).

Author contributions

Conceptualization: W.D., Z.X., and Z.Z.; Methodology: W.D., P.C., J.M., and P.S.; Investigation: W.D., P.C., J.M., P.S., J.H., Y.J., Q.L., H.W., Z.W., and W.W.; Visualization: W.D., P.C., J.M., P.S., Z.W., and W.W.; Funding acquisition: W.D., H.W., X.Z., Z.Z., W.W., and W.Z.; Project administration: W.D., H.W., X.Z., and Z.Z.; Supervision: X.Z., Z.Z., W.W., and Q.Z.; Writing – original draft: W.D., P.C., and J.M.; Writing – review & editing: Z.X. and Z.Z.

Competing interests

The authors declare no competing interests.

Additional information

Supplementary information The online version contains supplementary material available at <https://doi.org/10.1038/s41467-025-68057-w>.

Correspondence and requests for materials should be addressed to Zhi Zhang, Wei Wang, Qi-Xin Zhou or Xia Zhu.

Peer review information *Nature Communications* thanks Peng Cao and Congping Shang for their contribution to the peer review of this work. A peer review file is available.

Reprints and permissions information is available at <http://www.nature.com/reprints>

Publisher's note Springer Nature remains neutral with regard to jurisdictional claims in published maps and institutional affiliations.

Open Access This article is licensed under a Creative Commons Attribution-NonCommercial-NoDerivatives 4.0 International License, which permits any non-commercial use, sharing, distribution and reproduction in any medium or format, as long as you give appropriate credit to the original author(s) and the source, provide a link to the Creative Commons licence, and indicate if you modified the licensed material. You do not have permission under this licence to share adapted material derived from this article or parts of it. The images or other third party material in this article are included in the article's Creative Commons licence, unless indicated otherwise in a credit line to the material. If material is not included in the article's Creative Commons licence and your intended use is not permitted by statutory regulation or exceeds the permitted use, you will need to obtain permission directly from the copyright holder. To view a copy of this licence, visit <http://creativecommons.org/licenses/by-nc-nd/4.0/>.

© The Author(s) 2026